International Journal of Concrete
Structures and Materials

Experimental and Numerical Studies on the Mechanical Performance of a Wall-beam-strut Joint with Mechanical Couplers for Prefabricated Underground Construction

Tingjin Liu[1,2,3,4*] , Jiandong Lu[3] and Hongyuan Liu[4]

Abstract

This paper investigates the nonlinear behavior of wall-beam-strut joints with mechanical couplers, which are proposed for prefabricated underground constructions, under monotonic and cyclic loading conditions using full-scale experimental tests and three-dimensional finite element modelings. The nonlinear behavior of the joint is discussed in terms of the load–displacement curves, concrete cracking distributions, and strains in the reinforcements obtained from both the experimental tests and the numerical modeling. The comparison indicates that the trends of both load–displacement curves are similar, although the cracking, yield and ultimate loads of the joints determined by the numerical modeling are 2.5% lower, 2.6% higher and 3.8% higher, respectively, than those determined by the experimental tests. The numerical simulation can capture the concrete cracking process in the joint in the early loading stage but cannot accurately model the crack distribution in later stages. Moreover, the reinforcement strains and the skeleton curve from the numerical modeling show the same tendency as those from the experimental test, but it is difficult to compare their exact values, especially after yielding. The differences are believed due to the fact that the numerical modeling idealizes the materials and fails to model the slippage between the reinforcements and concrete after the concrete cracking. On the basis of the experimental and numerical investigations, it is concluded that the proposed wall-beam-strut joint has not only an ultimate bearing capacity that is at least 3 times higher than the design load but also a good ductility. Therefore, the design of the wall-beam-strut joint satisfies the requirements for the prefabricated underground construction.

Keywords: full-scale experimental test, finite element analysis, mechanical coupler connection, mechanical behavior, prefabricated underground construction

1 Introduction

In recent years, with the rapid urbanization in China, urban rail transit (UTR) has been quickly expanding due to its advantages of a large capacity, low energy consumption and environmental protection (Liu et al. 2019a). According to Liu et al. (2019b) and Zhang et al. 2019), UTR was operating in 34 cities in mainland China, and the total mileage reached 5055 km, which included 3884 km (77.2%) of subways, by the end of 2017. As an

*Correspondence: Liu_tingjin@163.com
[1] State Key Laboratory of Subtropical Building Science, South China University of Technology, Guangzhou 510640, China
Full list of author information is available at the end of the article

Liu *et al. Int J Concr Struct Mater*   (2020) 14:36

Page 2 of 23

important underground transportation system, subways reduce infrastructure at the ground level and play a significant role in mitigating traffic jams. A subway system consists of tunnels and metro stations. The most common construction method for the tunnels is the shield tunneling method, which is mechanized and automated, while the construction method of the metro stations is still the cast-in-place (CIP) method. As a traditional construction method, the CIP method has certain disadvantages, including creating water pollution, wasting a large amount of resources and requiring a long construction time, which are not consistent with the concept of sustainable development and green construction. Furthermore, Yang et al. (2019a) concluded that the disadvantages mentioned above would become particularly prominent in cold regions. Therefore, to overcome the construction difficulty, a new underground metro station construction method adapting prefabricated technology was proposed by Yang et al. (2019b). The basic concept of this metro station construction method borrows ideas from the shield tunneling. The single-ring metro station was divided into several prefabricated components, which were assembled together on site by grouting mortise–tenon joints. Moreover, Lu et al. (2018) and Xiu et al. (2018) reported another kind of prefabricated metro station construction method, which was used to construct the West Yanmazhuang Station of the Ji'nan Metro line 1 in China. Certain components of the supporting system for the foundation pit were prefabricated and became the permanent components when combined with the post-cast concrete. However, these approaches remain in the preliminary development stage, and abundant research needs to be done on this topic to ensure safe and durable structures.

Regarding the application of the prefabricated technology in aboveground and underground constructions, the strength of the connection joint is the most important factor. Thus, many scholars have conducted both experimental and numerical analyses to investigate the mechanical behavior of such joints. The most commonly used method for the dry connection is a mechanical reinforcement coupler. Bompa and Elghazouli (2018) conducted experiments to investigate the monotonic and cyclic mechanical behaviors of threaded reinforcement splices and demonstrated that the mechanical couplers exhibited good bearing capacity and ductility in both monotonic tests and cyclic tests. Furthermore, Bompa and Elghazouli (2017, 2019) investigated the inelastic cyclic behavior of reinforcement structures with mechanical coupler connections and pointed out that slender threaded couplers should be located in the plastic hinge zone to improve the ductility of the specimen.

Moreover, Chidambaram and Agarwal (2018) evaluated the performance of reinforced concrete beams with hybrid rebar coupler connections under monotonic loading, which revealed that coupler technology could avoid the buckling of longitudinal reinforcements when the couplers were located properly. Haber et al. (2014) conducted large-scale experiments to study the seismic performance of precast columns connected by two different kinds of mechanical couplers. The results revealed that the couplers had a significant impact on the plastic hinge mechanism but the overall performance of these columns with new connections was similar to that with CIP construction, which demonstrated the effectiveness of the mechanical couplers. Ameli et al. (2015) investigated the seismic response under cyclic loading of precast column-to-cap beam joints using grouted splice sleeve connections. The results showed that the precast joints with grouted splice sleeve connectors could satisfy drift capacity and displacement ductility requirements as well as CIP joints, which suggested that the grouted splice sleeve connectors were suitable and practical for accelerated bridge construction in the areas with moderate to high seismicities. Furthermore, some experimental studies on column-to-footing connections using grouted sleeves were conducted by Ameli et al. (2016). The results revealed that the seismic performance of the connection could be affected by the location of the grouted sleeves. Although the mechanical coupler connection has been reported to exhibit a favorable mechanical behavior, the differences among the performances in the different structural components remain unclear. Moreover, the investigations into the mechanical coupler connections used for underground construction are still lacking. The standard design method for the mechanical coupler connection is not applicable to the underground constructions, and the design in the underground constructions still depends mostly on the designers' experiences. Therefore, further studies, including both experiments and numerical simulations, are needed to investigate the mechanical coupler connection, especially in the emerging prefabricated underground construction.

Recently, Liu et al. investigated the mechanical performance of a diaphragm wall-waler beam-strut joint using a mechanical coupler connection for a prefabricated underground construction. Four full-scale experiments were conducted to investigate the strength and ductility of the joints subjected to static and cyclic loading conditions. Nevertheless, due to the time and cost limitations, it is impossible to conduct many full-scale tests with different loading conditions, which, however, can be conducted through numerical simulations.

Finite element method (FEM) is the most common numerical method used to analyze the nonlinear

Liu *et al. Int J Concr Struct Mater*   (2020) 14:36

Page 3 of 23

mechanical behavior of structures, with which many scholars simulate the nonlinear behavior of concrete coupled with the concrete damaged plasticity (CDP) model implemented in ABAQUS. For example, dos Santos et al. (2020) investigated the mechanical behavior of concrete-filled steel tubular columns with the CDP model and the influence of the stress–strain relationship for concrete. The numerical results slightly underestimated the mechanical behavior of the columns but the trends of the stress–strain curves agreed well with the experimental results. Wang et al. (2019) studied the mechanical performance of an improved precast prestressed beam-to-column joint through FEM with the CDP model, and the numerical results fit the experimental results well and helped to guide and improve the design of such joints. Nana et al. (2017) investigated the shear behavior of a reinforced concrete (RC) slab under concentrated loads and concluded that the results of the numerical modeling with the CDP model were in good agreement with the experimental results but overestimated the bearing capacity. Kazemi et al. (2020) carried out numerical simulations to investigate the nonlinear behavior of RC beams with glass-fiber-reinforced polymers (GFRP) and carbon-fiber-reinforced polymers (CFRP). With the CDP model, the numerical simulation predicted the failure of the beams well. In addition to the FEM modeling, the fiber element method can be used in the nonlinear analysis of reinforced concrete structures. Ameli and Pantelides (2017) proposed force-based beam-column elements to predict the mechanical behavior of precast concrete bridge columns with grouted splice sleeve connectors. The numerical results obtained using a plastic hinge modeling strategy agreed well with the experimental results. Wu and Pantelides (2018) used a fiber model and a rotational spring model to simulate the seismic performance of repaired column connections. Bond-slip spring elements were proposed to consider the slippage between the concrete and reinforcement. The computational results showed the effectiveness of two different models, especially the effectiveness of using the fiber model to reflect the pinching behavior of the structure.

As reviewed above, the FEM with the CDP model may predict the mechanical behavior of the RC structures well when reasonable parameters are chosen. Therefore, based on the experimental tests conducted by the author Liu et al., a three-dimensional numerical model is established in this paper using ABAQUS/Standard to investigate the mechanical performance of RC structures with a mechanical coupler connected joint. The outline of the article is as follows: Sect. 2 reviews the experimental test, introduces the specimen details and analyzes the experimental results briefly. Section 3 introduces the numerical model and the constitutive models of the concrete

and reinforcement. The comparison between the results from the experimental tests and numerical simulations is discussed in Sect. 3. Section 4 carries out a parameter analysis to investigate the effect of the mesh sensitivity, dilation angle and viscosity parameter on the obtained results together with the discussions of the effects of the axial compressive ratio and the longitudinal reinforcement diameter. Finally, Sect. 5 summarizes the conclusions drawn from this study.

2 Experimental Tests

Four full-scale wall-beam-strut joints were first constructed in the laboratory and then subjected to both monotonic and cyclic tests. Afterwards, the corresponding load–displacement curves and failure processes of the wall-beam-strut joints were analyzed.

2.1 Purpose of the Test

The author Liu et al. proposed a metro station construction method by adapting the prefabricated technology, which was implemented during subway construction in Guangzhou, China. In this method, in order to reduce the construction waste and improve the construction quality, some components of the station are prefabricated. As illustrated in Fig. 1, the components in a light-blue color are cast in the factory, which include the middle part of the beam, the slabs, and the platform slabs. The top slab of the station is a composite slab, which means that it is assembled with a CIP slab. The rest of the station is cast in place. Moreover, some members of the temporary supporting system are designed as permanent components, including the diaphragm wall, waler beam, and strut. Therefore, the connection strength and stiffness of the joint are vital. As shown in Fig. 2, the joint to be investigated consists of the diaphragm wall, the waler beam and a part of the strut. Because it is designed as a temporary component, the connection method is not clearly recommended by a standard or code; conventionally, the designer's experience determines how the components connect.

The most common connection method uses the postinstalled rebar. With a sufficient embedment length, a high-quality adhesive and skillful workers, this method can ensure the connection strength and thus is extensively used in aboveground constructions. However, limited by the underground construction conditions and the width of the wall, the postinstalled rebar connection method is not very useful in the construction of the metro station mentioned above. Correspondingly, the connection method of mechanical couplers is proposed for the construction of the station. As depicted in Fig. 3, the threaded sleeves are embedded in the wall by welding to the rebars during the casting of the wall.
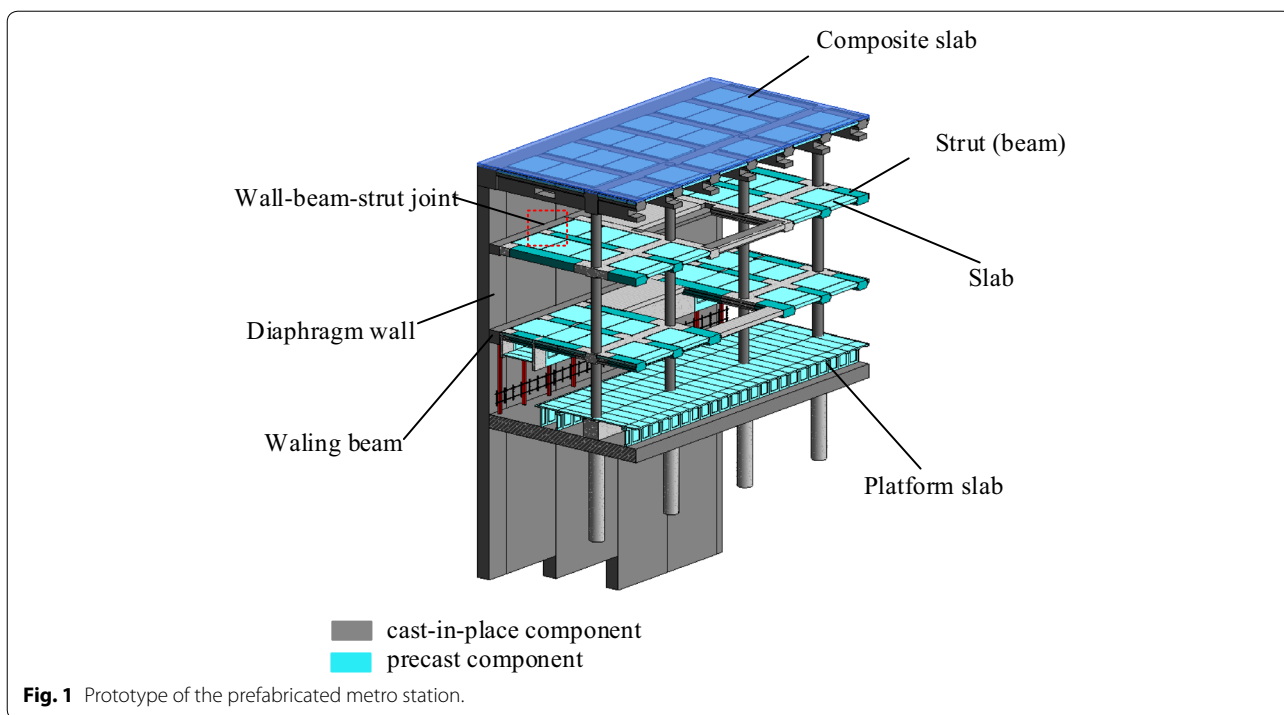
Liu *et al. Int J Concr Struct Mater*　(2020) 14:36

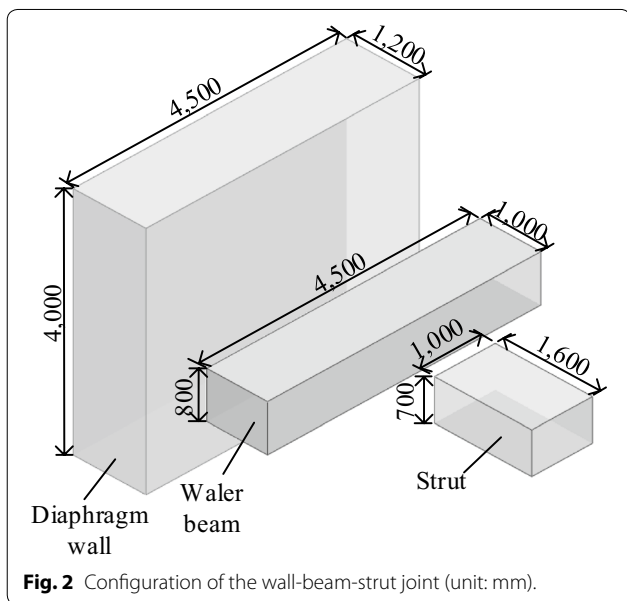Page 4 of 23
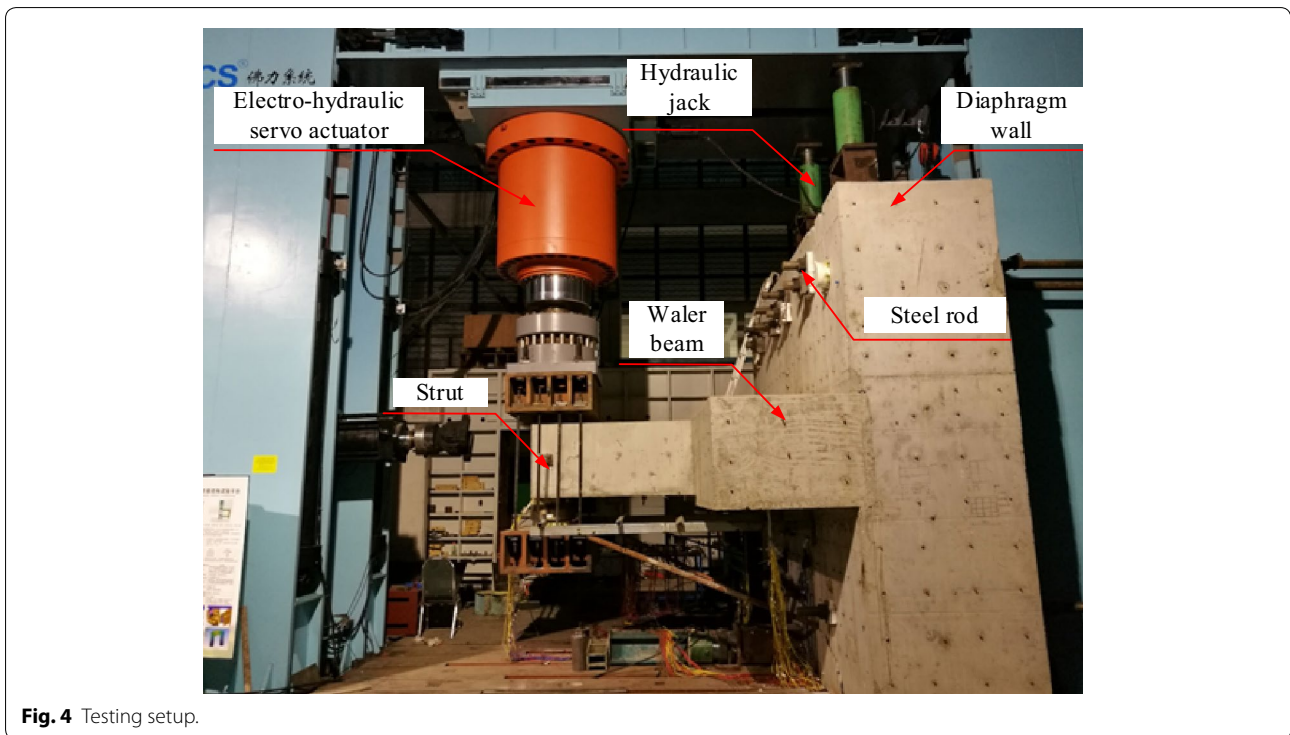

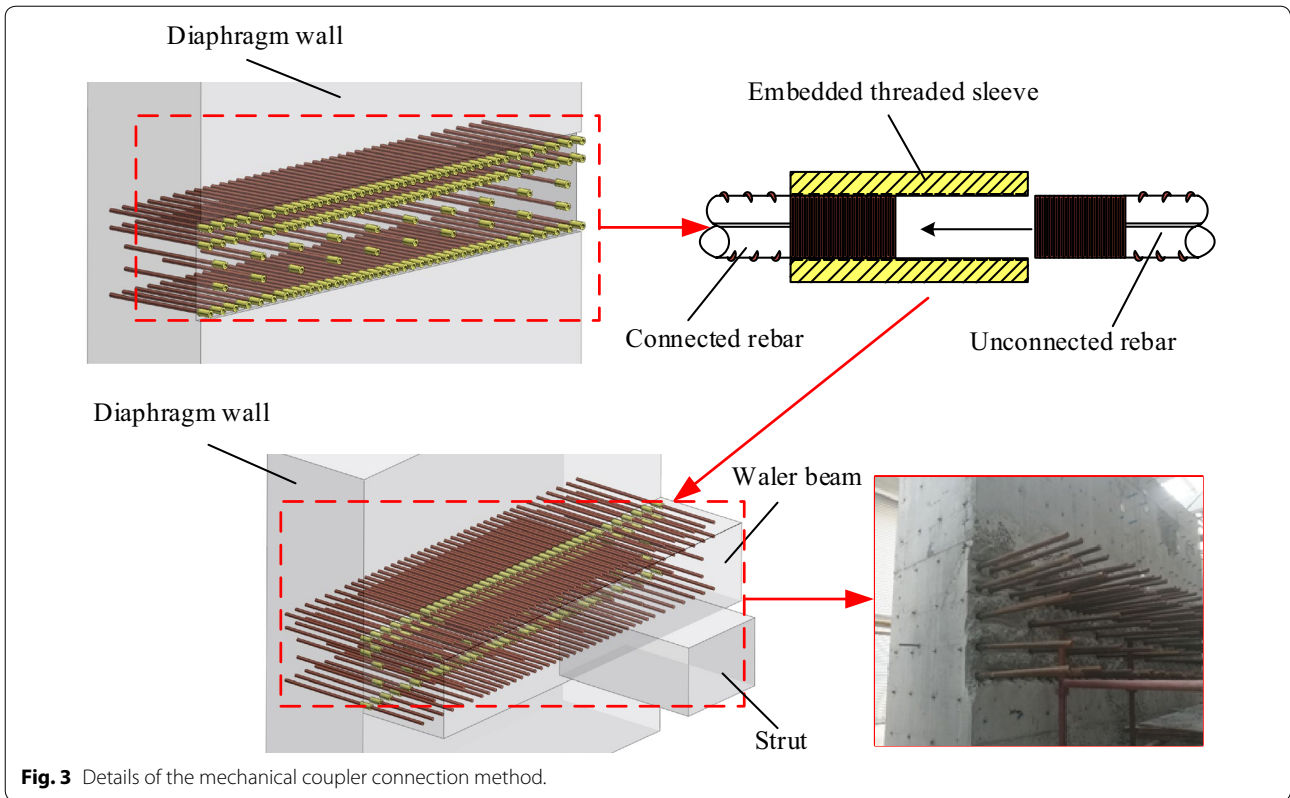**Fig. 1** Prototype of the prefabricated metro station.

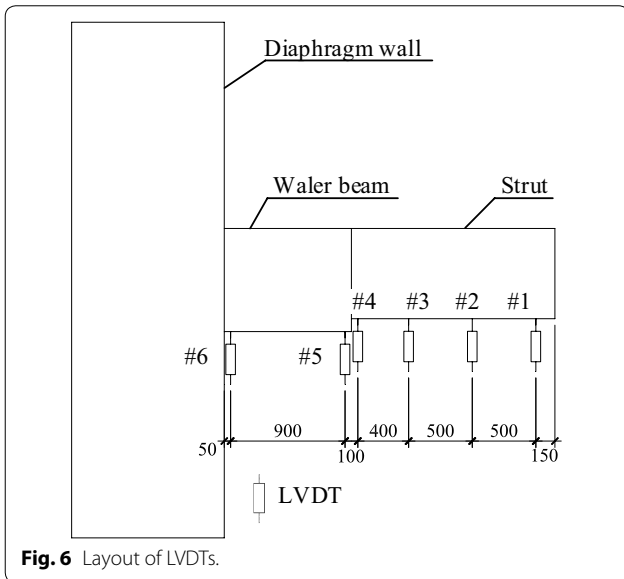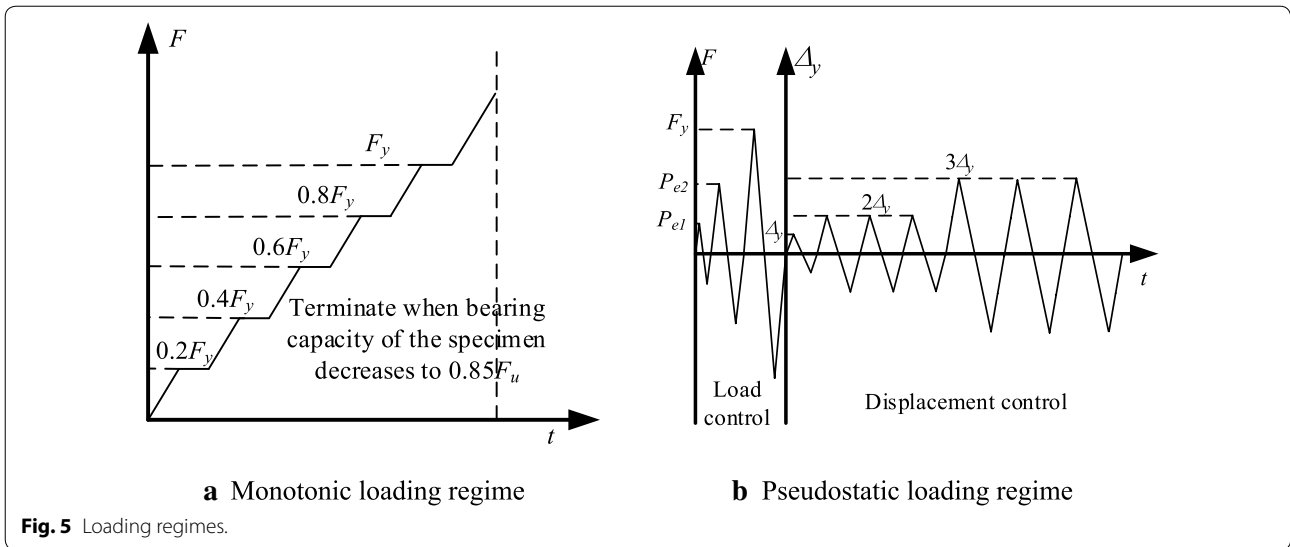**Fig. 2** Configuration of the wall-beam-strut joint (unit: mm).

Once the design strength of the wall concrete is satisfied, the concrete cover is chiseled out, and the anchor rebar in the waling beam is connected by the mechanical couplers. Due to its convenience in constructions, this method is widely used in the prefabricated structures. Most parts of the joints, for example, the column–column joint, are designed to be subjected to loads along the axis of the sleeves, which can ensure the strength of

the joint. However, the connection joint in a metro station will be subjected to loads perpendicular to the sleeve axis; thus, and the mechanical performance of the joint is unclear, and there is a lack of guidelines available for its design. Correspondingly, four full-scale experimental tests were designed by the author Liu et al. to investigate the mechanical properties of the joint.

2.2 Testing Setup and Instruments
To investigate the mechanical behavior of the joint under static and cyclic loading conditions, both monotonic loading and pseudostatic cyclic loading tests were carried out in the laboratory. Figure 4 shows the testing setup, in which the load was applied on the end of the strut by an electro-hydraulic servo actuator with a capacity of $+20,000$ kN (-5000 kN). The specimen was fixed in the vertical direction by the hydraulic jacks on the top of the wall and by the horizontal steel rods to prevent it from turning over during the test. The loading regimes used in the test were recommended by the Chinese Standard, as shown in Fig. 5. In the monotonic loading test, the load was increased step by step before the specimen yielded. After yielding, the load was increased continuously until the bearing capacity of the specimen decreased to 85% of the ultimate bearing capacity, which triggered the termination of the test. In the pseudostatic cyclic test, the loading was first controlled by the force loading condition but then switched to the displacement loading condition after the yielding of the specimen.

Liu *et al. Int J Concr Struct Mater*   (2020) 14:36

Page 5 of 23

Fig. 3 Details of the mechanical coupler connection method.

Fig. 4 Testing setup.

Liu *et al. Int J Concr Struct Mater* (2020) 14:36

Page 6 of 23

Fig. 5 Loading regimes.

Fig. 6 Layout of LVDTs.

To reflect the mechanical performance of the joint, the deflection of the strut, the strain of the rebars and the development of cracks were recorded during the test. As shown in Fig. 6, six linear variable differential transformers (LVDTs) were placed under the strut and the waler beam to measure the deflection at different positions. Moreover, several strain gauges were attached to the rebars in the specimen to record the changes in the rebar strain. As depicted in Fig. 7a, seven columns of strain gauges were attached to the vertical rebars of the diaphragm wall to measure the changes in the rebar strain in the core area of the wall. Moreover, to record the rebar strain in the waler beam, three rows of strain gauges were attached to the rebars in the waler beam, although only

the top row of the strain gauges could be seen in Fig. 7b. The other rows of strain gauges were named in the same way by replacing C1 with C2 and C3. Similarly, a series of strain gauges were placed on the longitudinal rebars and stirrups of the strut, as shown in Fig. 7c, d. To capture the mechanical behavior of the joint at other locations during the experiment, strain gauges were also installed on the second-row longitudinal rebars and the bottom compressive rebars, which are not shown in Fig. 7. These gauges were named using E and F, instead of D, to represent the second-row longitudinal rebars and bottom rebars, respectively.

2.3 Experimental Results
The monotonic loading tests focused on investigating the strut deflection, crack development, final pattern and bearing capacity of the wall-beam-strut joints. For the low-reversed cyclic loading tests, the hysteretic behavior and bearing capacity of the joints were observed, too. The corresponding results are described and discussed in the following sub-subsections.

2.3.1 Monotonic Loading Tests
Figure 8 presents the deflections of the cantilever part of the specimen at different positions under different loading levels. As illustrated in Fig. 8a, before the first-row longitudinal rebars of the strut yielded, the deflections at different positions increased linearly overall, and their increments decreased with the distance from the loading point increasing. After the yielding of the rebars, the deflections of the strut increased more rapidly and showed nonlinearity, indicating that the specimen yielded. Meanwhile, the deflections of the waler beam remained low, which implied that the wall and the beam
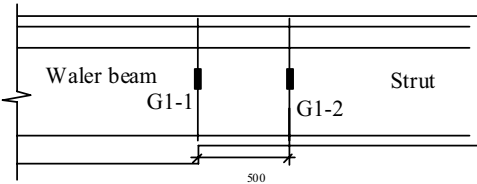
Liu *et al. Int J Concr Struct Mater*   (2020) 14:36

Page 7 of 23
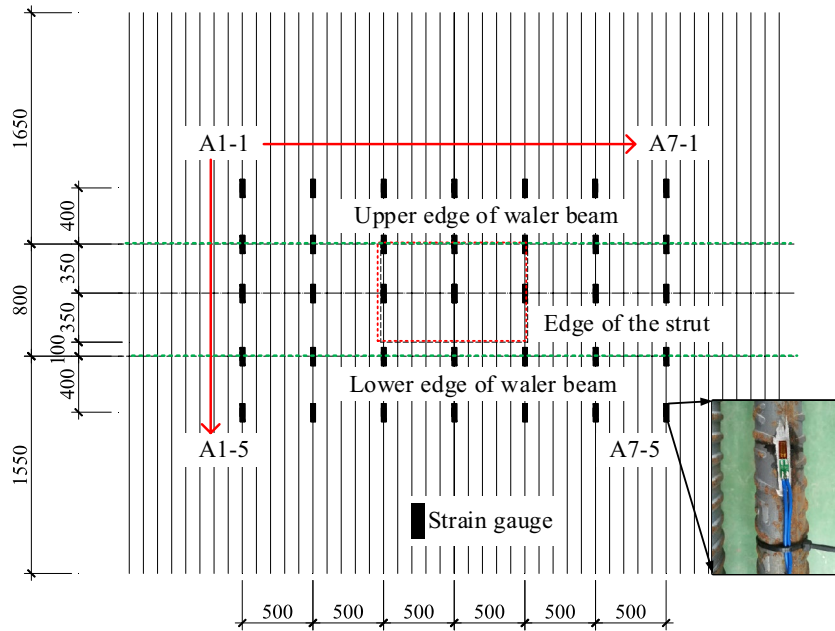
a Rebar strain gauges in the diaphragm wall
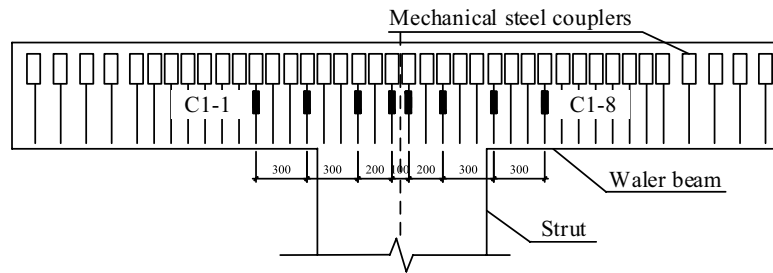
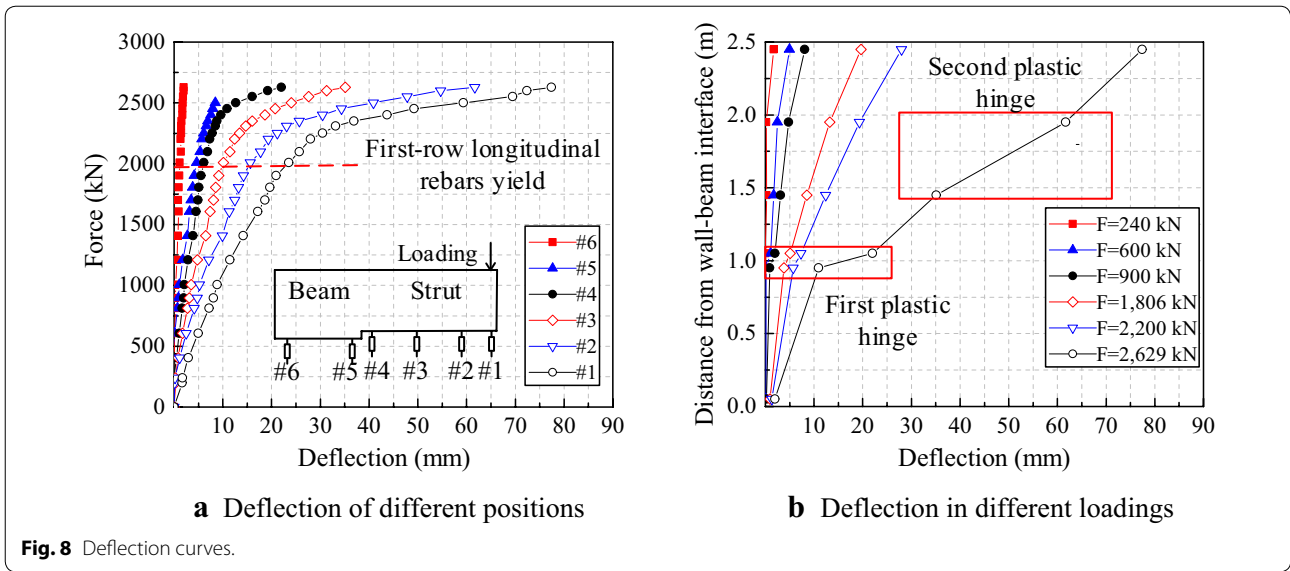**b** Rebar strain gauges in the waler beam
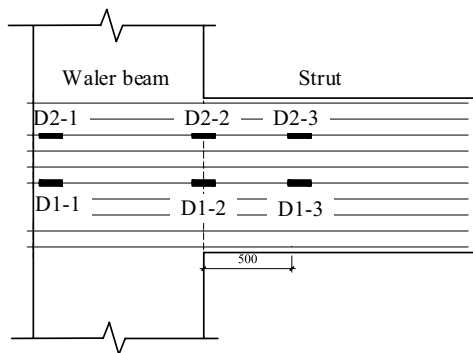
c Rebar strain gauges in the strut (longitudinal rebars)
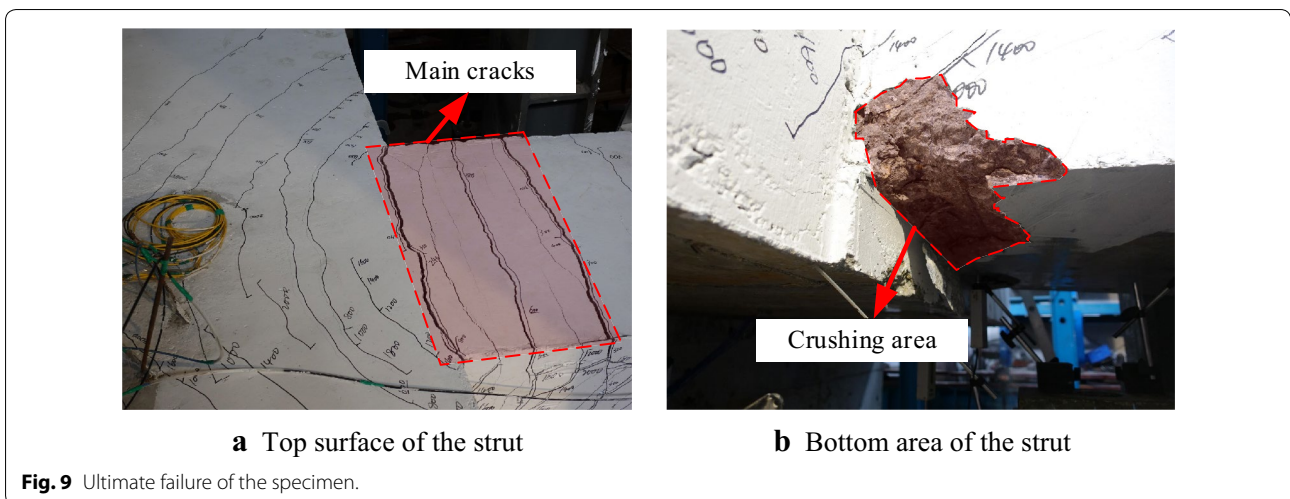
d Rebar strain gauges in the strut (stirrups)

Fig. 7 Layout of the strain gauges.
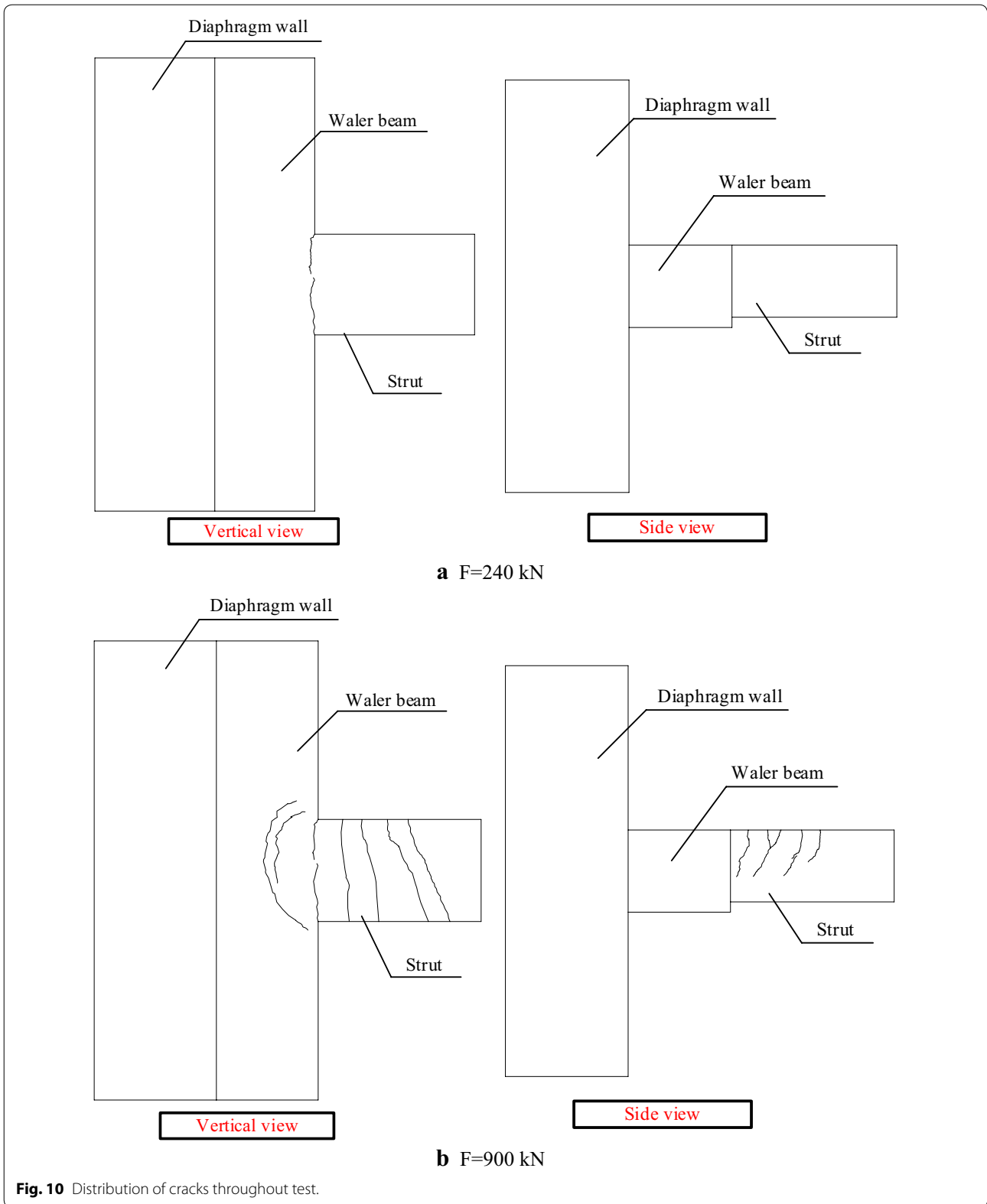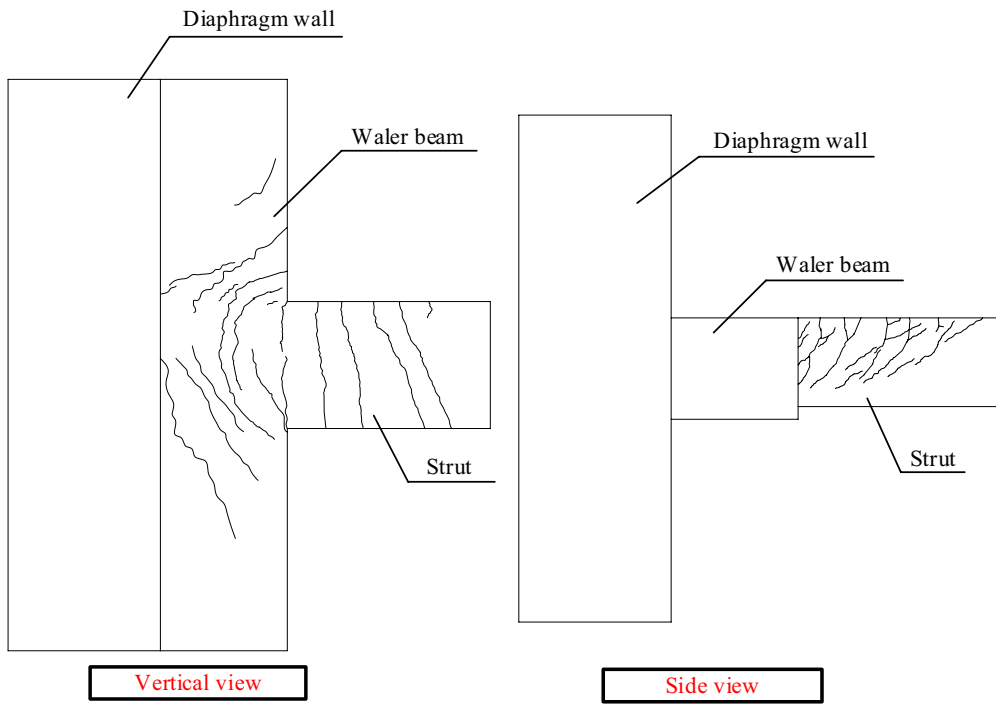
Fig. 8 Deflection curves.

could be considered as a fixed boundary when conducting some simple estimations. In addition, Fig. 8b revealed the relationship between the deflection and the distance from the wall-beam interface under different loading levels. Clearly, a certain turning point was present in each deflection curve as the loading increased. When the loading reached 2200 kN, this discontinuity in the deflection curve was approximately 1.0 m from the wall-beam interface. It could be inferred that the first plastic hinge was formed at the interface between the beam and the strut because the deflection curves of the strut remained linear and continuous. When the loading increased to 2629 kN, a second plastic hinge was formed in the middle of the strut, according to the turning point shown in the

deflection curve in Fig. 8b, which revealed the development of the plastic zone leading to the failure of the joint.
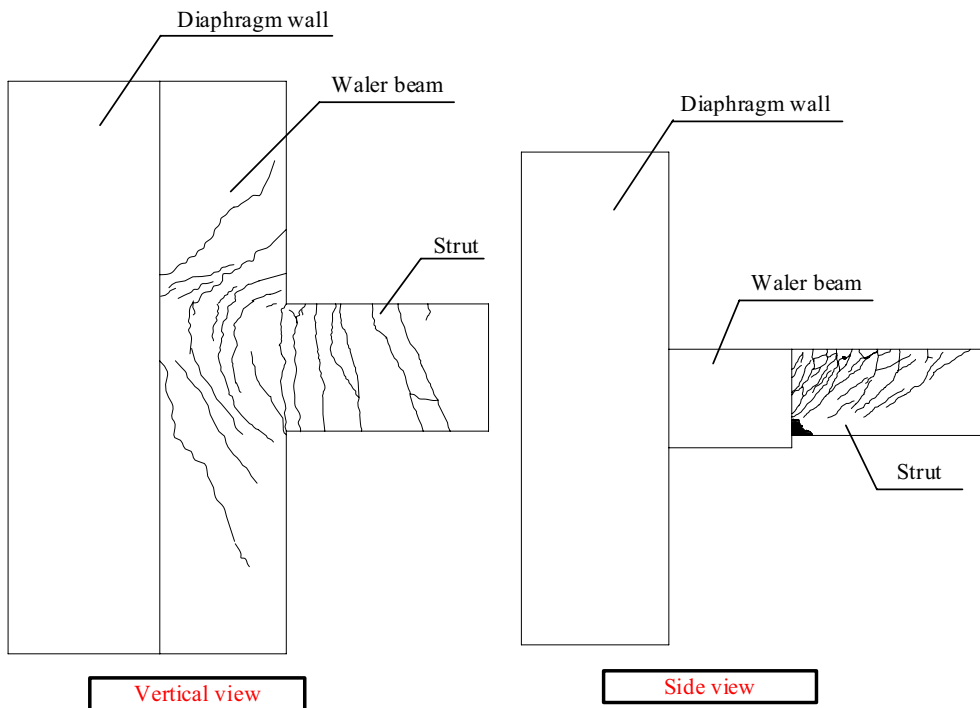
Figure 9 illustrates the ultimate failure pattern of the specimen. According to the measurements from the strain gauges before failure, tensile rebars yielded, and the joint retained its bearing capacity and showed good ductility. Nevertheless, the crushing of the concrete in the bottom of the specimen caused the joint to lose its bearing capacity immediately, which suggested that the failure of the joint was due to the crushing of the concrete in the bottom of the specimen. Furthermore, Fig. 10 presents the development of the cracks that were observed in the specimen. First, when the load was 240 kN, some cracks appeared along the top surface of the waler beam-strut interface, while no cracks appeared on the side surface of

Fig. 9 Ultimate failure of the specimen.

Liu *et al. Int J Concr Struct Mater*   (2020) 14:36

Page 9 of 23

Diaphragm wall

Waler beam

Strut

Vertical view

Diaphragm wall

Waler beam

Strut

Side view

a F=240 kN

Diaphragm wall

Waler beam

Strut

Vertical view

Diaphragm wall

Waler beam

Strut

Side view

b F=900 kN

Fig. 10 Distribution of cracks throughout test.

Liu *et al. Int J Concr Struct Mater*   (2020) 14:36

Page 10 of 23

c F=1,600 kN

d F=2,629 kN

Fig. 10 continued

the strut. As the load increased to 900 kN, more cracks were observed on the top surface of the waler beam and the strut, which included some semicircle cracks in the waler beam. The semicircle cracks revealed that the load severely affected the area and showed the load transfer path. Correspondingly, vertical cracks appeared on the side surface of the strut and developed along the oblique direction. Then, as the load increased to 1600 kN, the cracks on the top surface of the waler beam extended to the waler beam-diaphragm wall interface. More small cracks branched from the ends of the cracks on the side surface of the strut, and these cracks extended to the loading point. Finally, when the load reached 2629 kN, the crushing of the bottom concrete caused the failure of the specimen. Compared with the crack development in the previous stage, the development of the cracks on the top surface of the strut was not obvious. However, the cracks on the side surface of the strut developed and intersected quickly, and the number of cracks increased rapidly. From the deflection of the strut shown in Fig. 8b, it could be inferred that the considerable increase in the number of the cracks on the side surface represented the formation of the second plastic hinge in the middle of the strut.

2.3.2 Low-Reversed Cyclic Loading Test

Figure 11 depicts the final failure pattern of the specimen under the low-reversed cyclic loading condition, which indicated that the crushing of the concrete in the top area of the waler beam caused the joint to fail. When the joint was subjected to a displacement loading equal to twice the yielding displacement in the positive direction, some reinforcements fractured and made a loud noise, which led to the loss of the bearing capacity in the positive direction. Nevertheless, considering the cost of

the experiment, the load was continuously applied in the negative direction until the specimen failed completely. The cracks caused by the positive and negative loads are highlighted by red and black lines, respectively, in Fig. 11, which were mutually symmetric and similar to those observed in the monotonic loading test. Moreover, the ultimate bearing capacity recorded in the cyclic loading test was similar to that obtained in the monotonic loading test, as shown in Fig. 12, although the ultimate bearing capacity in the negative direction of the cyclic tests was smaller than that in the positive direction. The difference between the ultimate bearing capacities in the positive and negative directions was mainly caused by the different number of the longitudinal reinforcements. As shown in Fig. 7d, there were two rows of reinforcements in the top area of the strut but only one row of
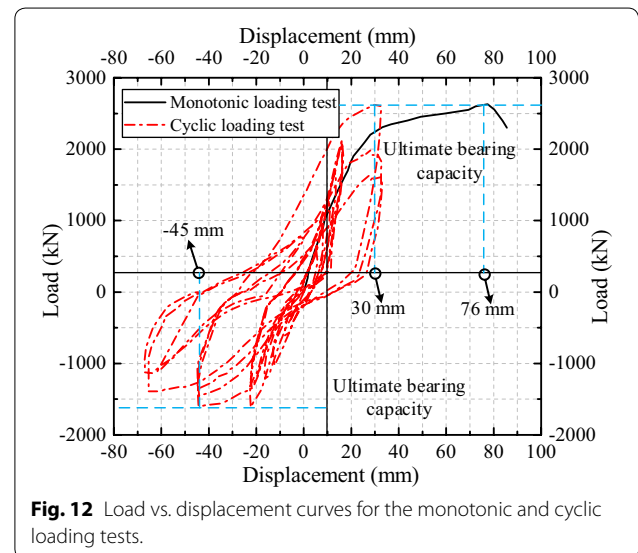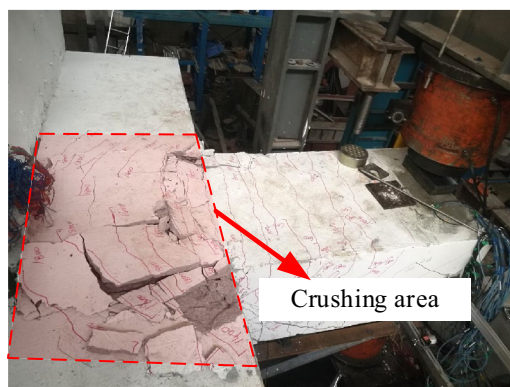

Fig. 12 Load vs. displacement curves for the monotonic and cyclic loading tests.

a Top surface of the strut   **b** Side surface of the strut

Fig. 11 Ultimate failure of the specimen.

Liu *et al. Int J Concr Struct Mater*   (2020) 14:36

Page 12 of 23

reinforcements in the bottom area. During service, the top and bottom areas were expected to bear tensile and compressive loads, respectively, which was why the number of the longitudinal reinforcements in the top area was larger than that in the bottom area. Furthermore, the ductility performance varied because of the damage accumulation under the cyclic loading conditions. In the monotonic loading test, the ultimate displacement corresponding to the ultimate bearing capacity was recorded as 76 mm. The ultimate displacements obtained from the cyclic loading test in the positive and negative directions were 30 mm and -45 mm, respectively, which were far less than those obtained from the monotonic test. It could be inferred that the ductility of the specimen decreased under the cyclic loading conditions because of the accumulation of the concrete damage.

3 Nonlinear Numerical Analysis

In this section, three-dimensional finite element models were first built to investigate the failure processes and mechanical properties of the tested specimen under static and cyclic loading conditions with ABAQUS/Standard. The obtained results from the numerical modeling were then compared with those obtained from the experimental tests.

3.1 Numerical Model and Boundary Conditions

Eight-node hexahedral elements with reduced integration (C3D8R) were used for simulating the concrete, and two-node linear truss elements (T3D2) were adopted for the rebars. Considering the calculation time and efficiency,

the average mesh size was set to be approximately 100 mm. Correspondingly, the total number of nodes and elements in the numerical model were 44,543 and 45,522, respectively. A desktop computer with 32 GB memory (RAM) and a 3.40 GHz Core i7-6700 CPU was used for the analyses. It is very important to model the interaction between the reinforcement and concrete. In this study, the embedded element technique was used, which meant that the perfect bond between the reinforcement and concrete was considered. The concrete was the "host", while the rebars were embedded, as depicted in Fig. 13a, b, respectively. Normally, the strength of mechanical couplers is higher than that of rebars. Therefore, the mechanical couplers were neglected, and the rebars between the wall and the waler beam were continuous to simplify the numerical model.

To compare the numerical results with those from the experiments, the boundary and loading conditions of the numerical model were the same as those in the experimental tests. Figure 14 illustrates the boundary and loading conditions for the numerical modeling. Both side surfaces of the diaphragm wall were constrained in the y-direction, the top surface was constrained in the x-direction, and the bottom surface was an encastre boundary. To apply the loading, a loading reference point was first created, and the top surface of the block was then coupled with the point. Afterwards, the displacement loading was applied at the point, which was the same location as that in the experimental loading regimes. Moreover, the pattern of the displacement
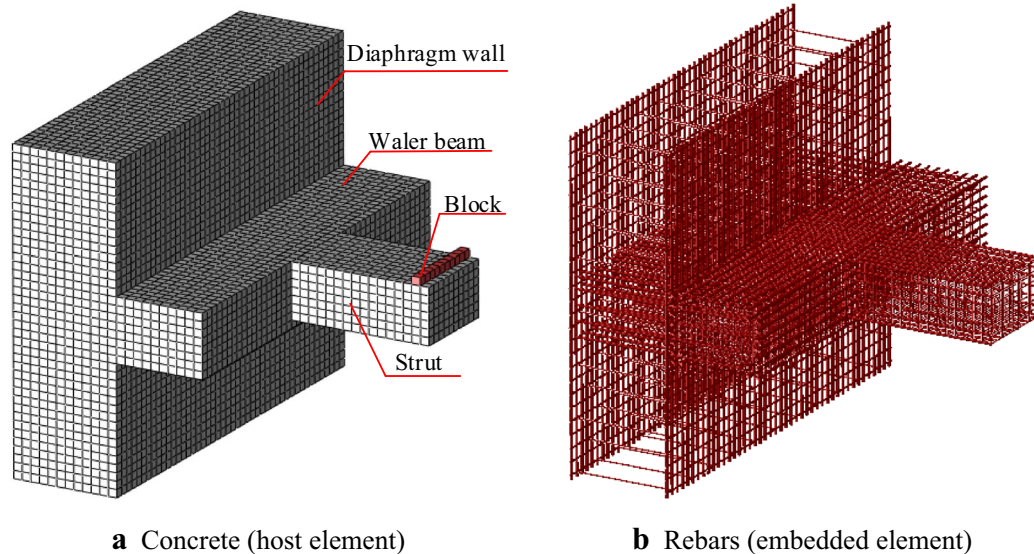

a Concrete (host element)　　　　**b** Rebars (embedded element)

Fig. 13 Host element and embedded element.

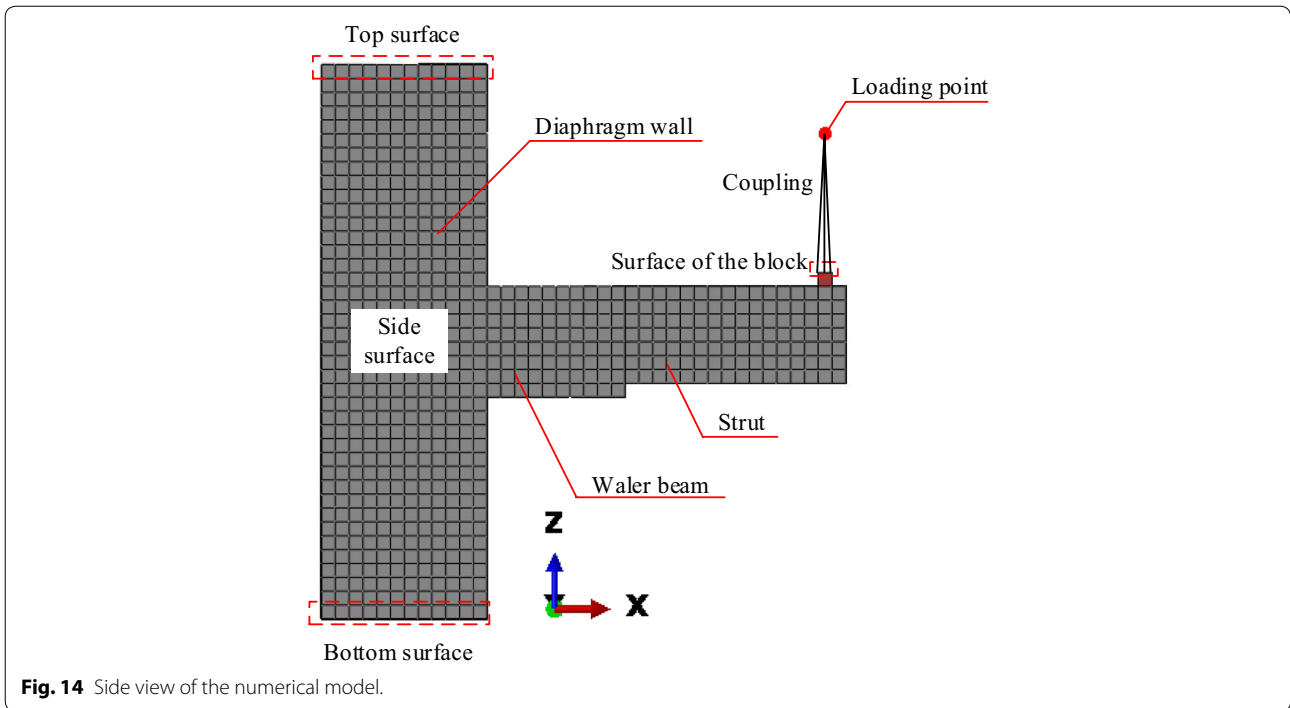Liu *et al. Int J Concr Struct Mater*   (2020) 14:36

Page 13 of 23

Fig. 14 Side view of the numerical model.

loading curve applied in the numerical modeling was the same as that used in the experimental test.

3.2 Constitutive Models of the Concrete and Reinforcement

One of the most significant factors affecting the numerical result is the constitutive model of the material used in the computational model. In this paper, the constitutive models of the concrete and reinforcement are vital to the

numerical results. Therefore, they are described and discussed in the following sub-subsection.

3.2.1 Constitutive Model of the Concrete

The constitutive model of the concrete recommended by the code for the design of concrete structures (GB 50010-2010) in China was used in the numerical modeling. As shown in Fig. 15, the constitutive model could be divided into tensile and compressive parts. In terms of the tensile part, the stress–strain relationship remained linear before
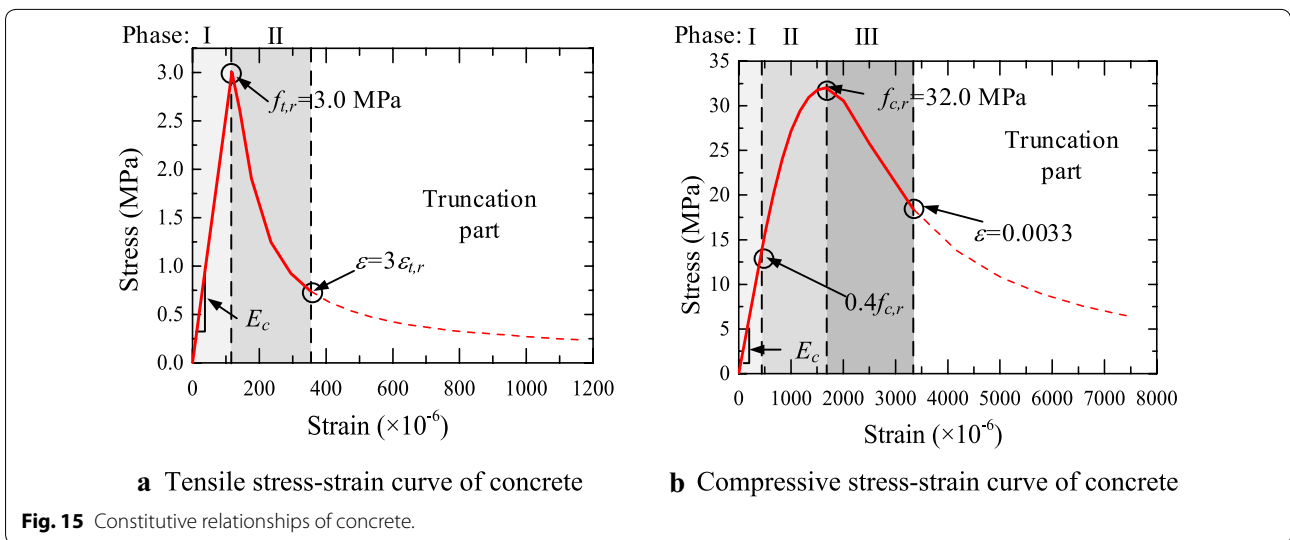

a Tensile stress-strain curve of concrete

b Compressive stress-strain curve of concrete

Fig. 15 Constitutive relationships of concrete.

Liu *et al. Int J Concr Struct Mater* (2020) 14:36

Page 14 of 23

Fig. 16 Damage variables.
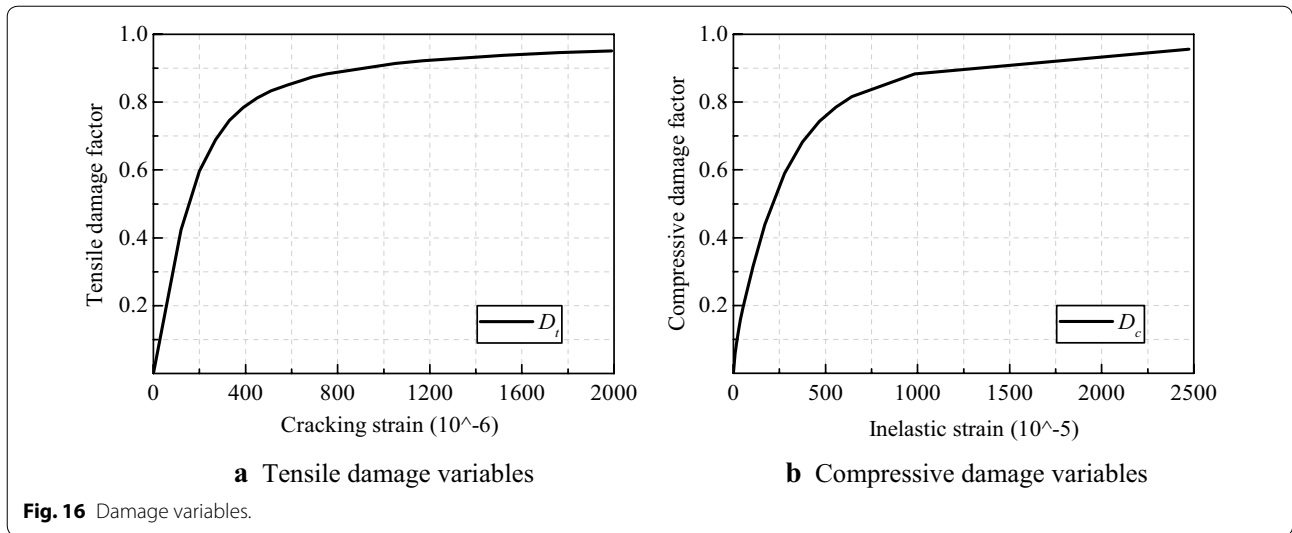
Table 1 Parameters of the CDP model for concrete.

| ψ	ε	σ_{b0}/σ_{c0}	K_c	μ
30°	0.1	1.16	0.667	0.01

the stress reached the peak tensile strength $f_{t,r}$ and then showed a nonlinear behavior in the postpeak branch. To truly represent the failure of the concrete, the curve should be truncated at three times the strain observed at the peak tensile stress $\varepsilon_{t,r}$. For the compressive part, the stress increased linearly with the strain before reaching the elastic limit $0.4f_{c,r}$. Afterwards, the stress nonlinearly increased to the peak compressive strength $f_{c,r}$. In the descending branch, the behavior was similar to that of the tensile part, and the curve should be truncated at the ultimate compressive strain ε_{cu}.

In this paper, the CDP model provided by ABAQUS/Standard was adopted to describe the nonlinear damage behavior of the concrete. Combined with the equivalent energy method proposed by Sidoroff (1981), the damage variables were derived, and Fig. 16 shows the calculated results. The other parameters used for the CDP model are listed in Table 1. Moreover, the influence of the dilation angle ψ and viscosity parameter μ on the numerical results are discussed later. The potential flow eccentricity ε, the ratio of the equibiaxial compressive yield stress to the uniaxial compressive yield stress σ_{b0}/σ_{c0} and the ratio of the second stress invariant to the tensile meridian K_c were set as the default values in this paper.

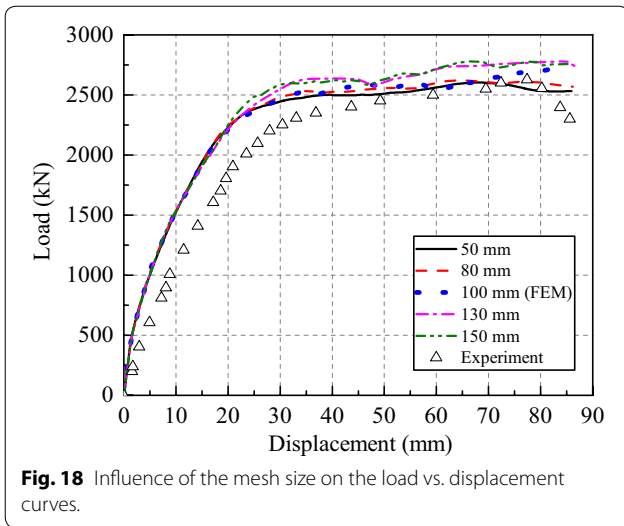### 3.2.2 Constitutive Models of the Rebars

To represent the uniaxial mechanical behavior of the rebars, a bilinear model was used in this paper. As

Fig. 17 Constitutive model of the reinforcements and the steel plate.
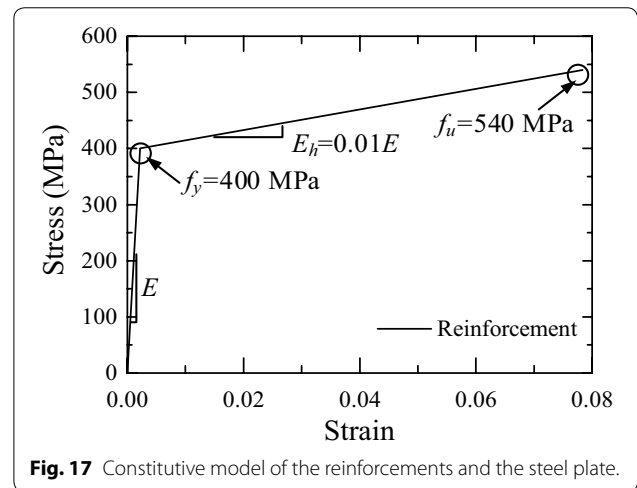
illustrated in Fig. 17, the elastic phase of the material could be described by Young's modulus E and the yield load f_y. After the stress reached the yield load, the stress would increase to the ultimate load with a hardening modulus E_h, which was assumed to be 1% of Young's modulus E. The Young's modulus and the yield load of the rebars were 183 GPa and 400 MPa, respectively.

3.3 Mesh Sensitivity Analysis

To ensure the accuracy of the numerical results, mesh sensitivity analysis was performed in this paper. Five mesh sizes, namely, 50 mm, 80 mm, 100 mm (used in the above analysis), 130 mm and 150 mm, were implemented in the numerical analysis to investigate the effect of the mesh on the numerical results. Figure 18 shows that the differences among the numerical results were

Fig. 18 Influence of the mesh size on the load vs. displacement curves.

Table 2 Ultimate bearing capacity and calculation time with different mesh sizes.

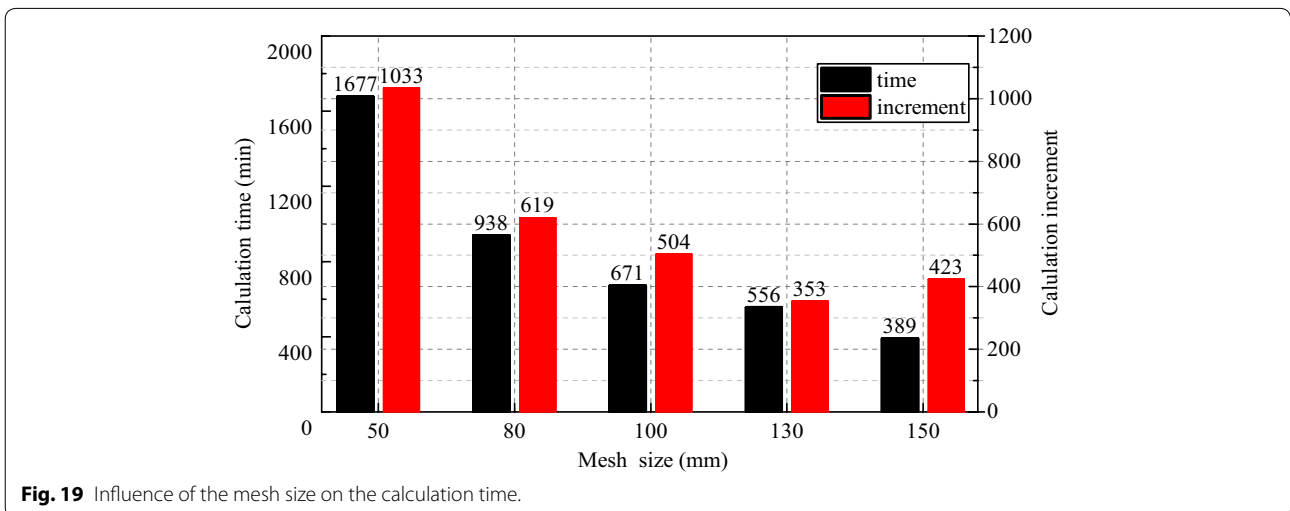| Mesh size (mm)	50	80	100	130	150
Ultimate bearing capacity (kN)	2605	2776	2942	2808	2939
Relative error (%)	− 0.93	− 0.33	− 3.85	7.70	9.07

while attempting to converge and needed more increments to satisfy the convergence requirements. Furthermore, a finer mesh increased the number of elements and nodes and the size of the computational matrixes, which required more computational time to solve. When the mesh size was smaller than 100 mm, the relative error was below 1%. However, the calculation time increased rapidly as the mesh size decreased. Moreover, when the mesh size varied from 50 mm to 100 mm, the differences among the results were negligible. Therefore, the chosen mesh size was sufficient for the numerical modeling presented above.

3.4 Numerical Modeling Results and Comparison with those from the Experiments

In order to further verify the accuracy of the numerical model, the loading vs. displacement curves, crack patterns, reinforcement strains, and skeleton curves obtained from both experimental tests and numerical simulations are compared qualitatively and quantitatively, which are presented in the following sub-subsections.

3.4.1 Loading vs. Displacement Curves

Figure 20 compares the load vs. displacement curves of the joint determined from both numerical analysis and experimental test. In general, they agreed well with each other, although the stiffness from the numerical

not obvious before the specimen yielded. After yielding, as the mesh size increased past 100 mm, the peak load of the specimen increased. Moreover, the numerical specimen exhibited a larger stiffness as the mesh size increased. Figure 19 and Table 2 show the calculation times and the ultimate bearing capacities, respectively, from the numerical modeling with different mesh sizes. The relative error was calculated in comparison with the experimental testing results, which is listed in Table 2. To a certain extent, the number of calculation increments indicates the convergence rate of the numerical modeling in ABAQUS. A larger number of increments indicates a slower convergence rate when the other computation conditions, such as total loading magnitudes, are kept the same. Therefore, as illustrated in Fig. 19, with a finer mesh, the computational time increased. The numerical modeling with a finer mesh experienced more difficulty

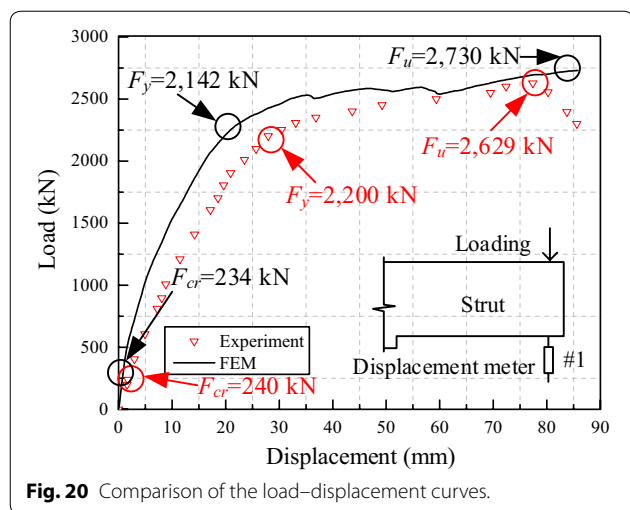**Fig. 19** Influence of the mesh size on the calculation time.

Fig. 20 Comparison of the load–displacement curves.

Table 3 Comparison of results.

Value	Cracking load (kN)	Yielding load (kN)	Ultimate load (kN)
Experimental result	240	2200	2629
Numerical result	234	2142	2730
Relative error (%): $e = |(F_e - F_n)/F_e|$	2.5	2.6	3.8

modeling was higher than that from the experimental test. Moreover, the ductility obtained from the FEM model seemed to be also higher than that from the experimental test. These differences could be that the materials, including the concrete and rebars used in the FEM model were idealized, and that the discreteness of the materials was neglected. In addition, during the loading process in the experimental test, the loading was temporarily stopped to record the location and width of the generated cracks when they reached certain magnitudes. Therefore, the damage in the joint might have accumulated after the specimen yielded, but this did not happen in the numerical simulation, which was another source resulting in these differences. However, Table 3 shows the cracking load calculated from the FEM model was only 2.5% smaller than that from the experimental test. The yielding load obtained from the FEM model was very close to that from the experiments. Moreover, the maximum relative error between the ultimate loads from the numerical modeling and the experimental test was only 3.8%, which was still under 5%. Therefore, the numerical results were acceptable and could capture the failure characteristics of the joint.

3.4.2 Crack Distributions

According to the CDP model, the crack distribution in the specimen can be approximately described by the development of tensile damage. The development process of tensile damage is illustrated in Fig. 21. When the load increased to 240 kN, a crack first appeared at the interface between the waler beam and the strut, while no cracks were observed on the side surface of the strut. As the load increased to 900 kN, additional cracks were observed on the top surface of the strut, and some semi-circle cracks were observed on the top surface of the waler beam, in both the FEM model and experimental test. In the FEM model, tensile damage occurred at the interface between the diaphragm wall and waler beam. However, no cracks were observed on the surfaces of the wall in the experimental test. In the experimental test, the beam and the strut were cast after the wall satisfied the design strength. In other words, a construction joint existed between the wall and the beam. However, to simplify the FEM model, the effect of the construction joint was neglected; and the simplification of the connection between the diaphragm wall and the waler beam might have caused the differences between the experimental and numerical results. Figure 21c shows that, when the load increased to 1600 kN, the distribution of the tensile damage in the FEM model could not describe the crack distribution any longer because of the accumulation of the tensile damage. Nevertheless, the distribution of the tensile damage could still indicate the area of cracking development. Notably, a uniform mesh size was adopted to exclude the effect of mesh size on the damage distribution. However, a denser mesh may be used around the joint to model the cracking pattern in greater detail.

3.4.3 Strain on Reinforcements

Figure 22 compares the strains on the reinforcements monitored in different parts of the strut from the experimental test and numerical analysis. The experimental results were plotted with hollow markers, while those from the numerical analysis were plotted with a solid line. As shown in Fig. 22, most of the strains in the different parts of the strut obtained from the FEM model showed the same tendency as those from the experimental test. Moreover, the strains were sometimes very similar. A comparison between Fig. 22a, b indicates that both the first-row and the second-row rebars yielded at the same time at the beam-strut interface, which led to the yielding of the specimen. As the load increased, the strains of D1–3, D2–3 and E1–3 and E2–3 also increased to the yielding strain, which indicated the development of the plastic zone. Moreover, as seen in Fig. 22d, after the specimen yielded, the strain of G1–2 increased rapidly
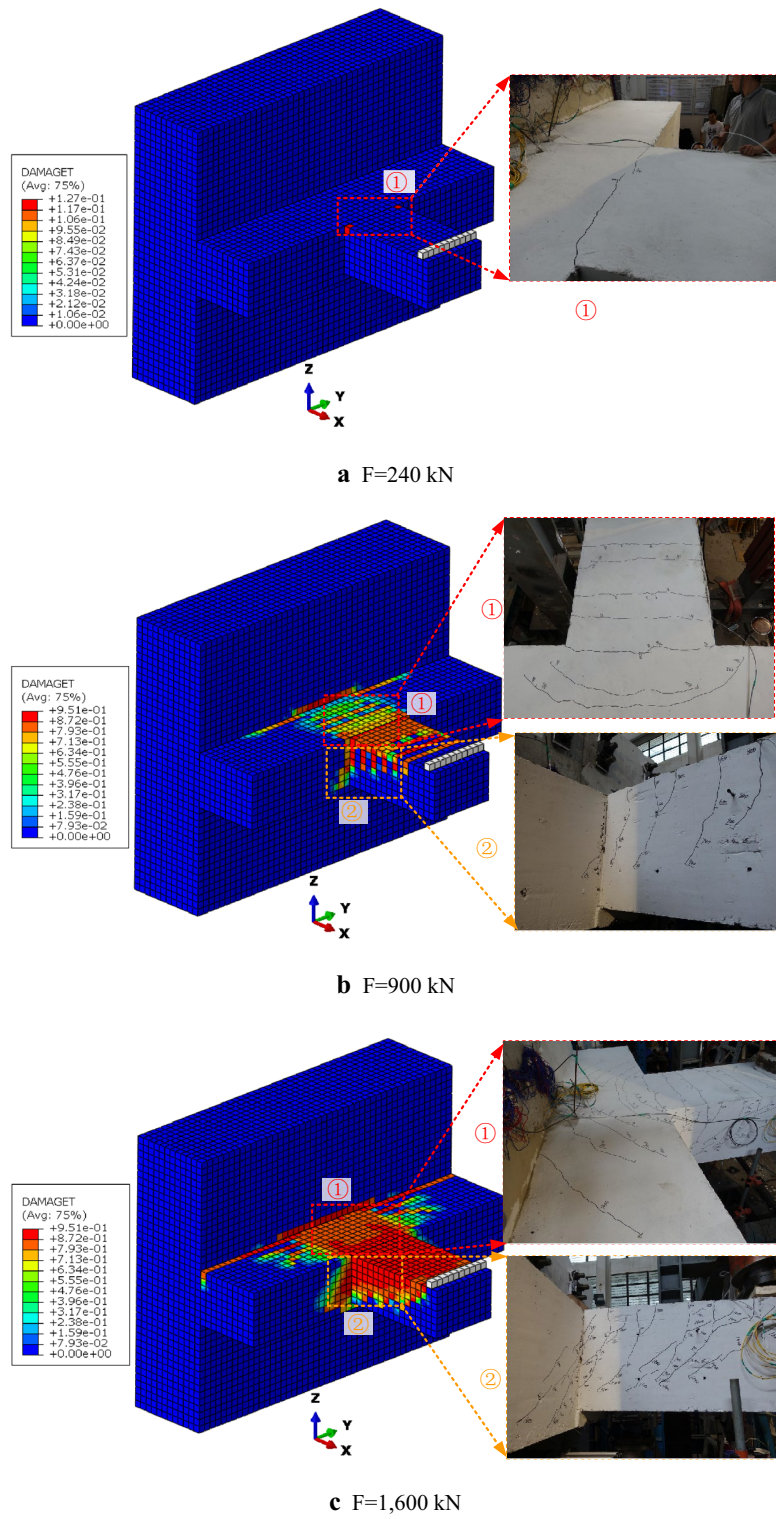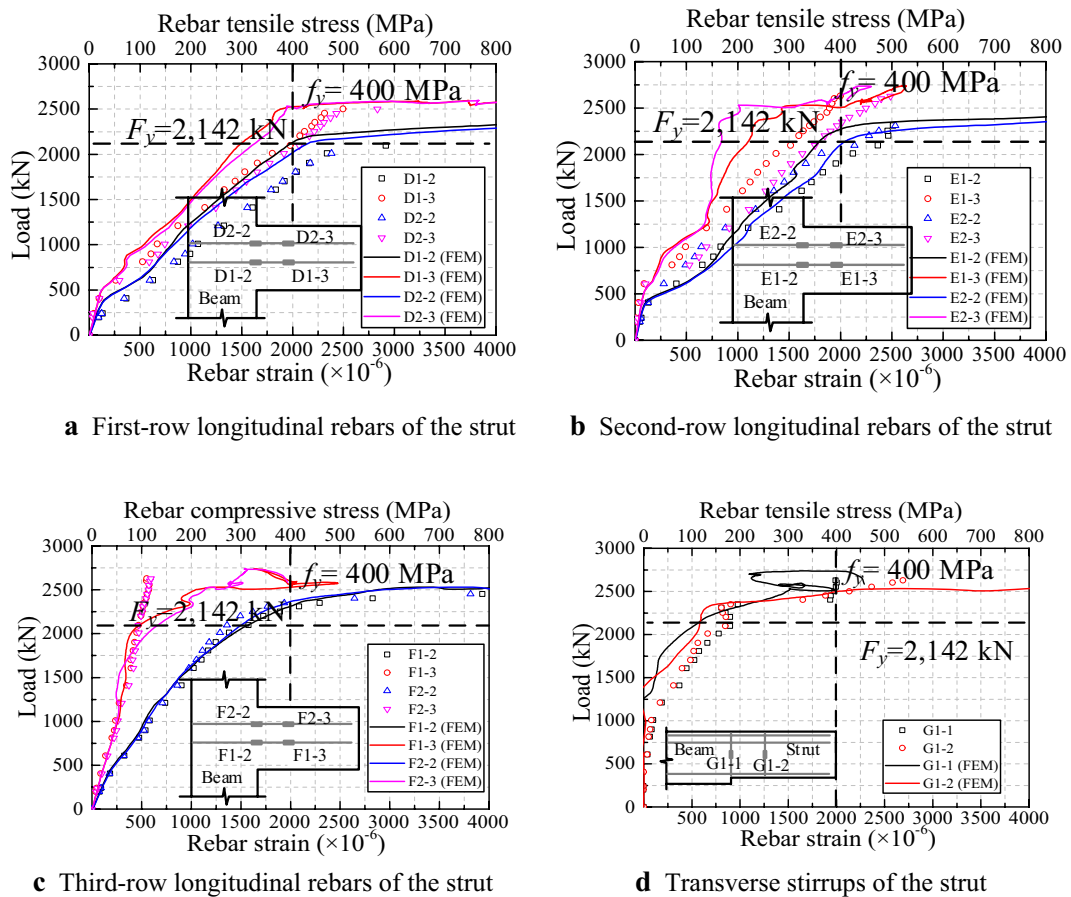
Liu *et al. Int J Concr Struct Mater*   (2020) 14:36

Page 17 of 23

Fig. 21 Comparison of crack distributions.

Liu *et al. Int J Concr Struct Mater*   (2020) 14:36

Page 18 of 23

Fig. 22 Comparison of the strains on the reinforcements.

a First-row longitudinal rebars of the strut

b Second-row longitudinal rebars of the strut

c Third-row longitudinal rebars of the strut

d Transverse stirrups of the strut

to the yield strain, suggesting that the second plastic hinge was formed in this area. This observation explained why the cracks on the side surface of the strut increased rapidly, as observed in the late loading stage during the experimental test. However, in this stage, because of the differences in the load distribution inside the concrete, the inaccurate position of the strain gauges and so on, the strain results of the rebars from the numerical modeling diverged slightly from those obtained from the experimental investigation. Overall, the numerical modeling could still represent the loading progress of the specimen in the experimental test to a great extent.

3.4.4 Skeleton Curve

Figure 23 presents the skeleton curve obtained from the FEM model, which indicates a greater stiffness than that obtained from the experimental test. The skeleton curves were drawn by connecting the maximum loading points of the hysteretic curve obtained in each cycle of the cyclic test. For example, the experimental skeleton curve in Fig. 23 was drawn by connecting the maximum
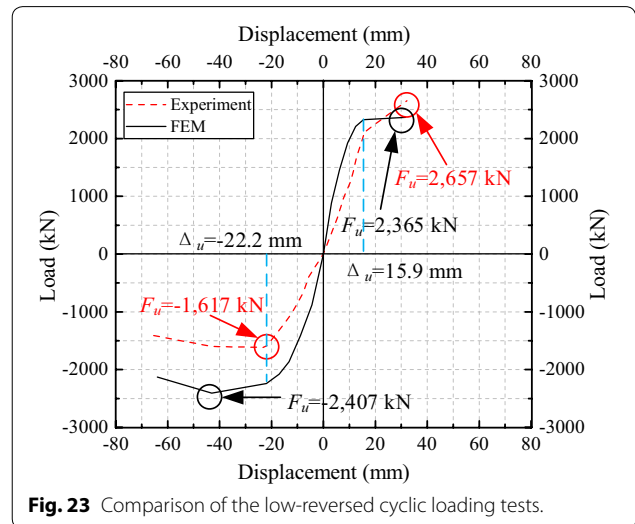

Fig. 23 Comparison of the low-reversed cyclic loading tests.

loading points of the hysteretic curves, i.e., the red dashed curves, in Fig. 12. In the positive direction (+), the ultimate load obtained from the numerical results

Liu *et al. Int J Concr Struct Mater*   (2020) 14:36

Page 19 of 23

was 2365 kN, which was approximately 11% smaller than that from the experiment. Moreover, in the experimental test, some rebars fractured when the loading displacement was equal to twice the yielding displacement, which caused the specimen to lose its bearing capacity in the positive direction and the termination of the loading stage. However, the numerical results did not show the descending tendency, and the numerical specimen retained its bearing capacity. On the other hand, the ultimate load from the numerical modeling of the monotonic loading test was close to that from both the monotonic and cyclic experimental tests. Therefore, it could be inferred that the accidental fracturing of the rebars caused the specimen to reach its ultimate load and lose its bearing capacity early. In the negative direction (−), the differences in the bearing capacities between the numerical modeling and the experimental tests seemed to be larger because the fracturing of the rebars and formation of the tensile cracks observed on the top surface of the strut had a great influence on the bearing capacity in the negative direction (−). Moreover, the slippage between the concrete and the rebars after the concrete cracking was neglected in the numerical modeling, which caused the numerical model to present a higher stiffness. This limitation may be overcome by the phenomenological model proposed in the literatures (Ameli and Pantelides 2017; Wu and Pantelides 2018), which will be the focus of our future work. Despite the differences, the trends of the skeleton curves from the FEM model and the experimental test generally agreed well with each other. However, only the skeleton curves were compared here while the hysteretic curves from the FEM model and the experimental test were omitted, which would be discussed in future studies.

4 Discussion

Section 3 compares the nonlinear mechanical behaviors of the wall-beam-strut joints under the monotonic and cyclic loads obtained from both numerical modeling and experimental testing. The good agreement between the results reveals the accuracy and reasonability of the numerical modeling approach. As a further in-depth analysis, parametric analyses were conducted to discuss the effect of some important parameters on the obtained results. Moreover, the mechanical behavior of the joints under different loading conditions is discussed in this section, too. Since the numerical modeling of the cyclic loading test is rather time-consuming without using a supercomputer, the parametric analyses were conducted only for the monotonic loading test.

4.1 Effect of the Dilation Angle

According to the ABAQUS user's manual (2016), the dilation angle can affect the plastic flow potential function. Wosatko et al. (2019) concluded that the dilation angle could control the shape of the plastic potential surface, which would become increasingly broader with the rise in dilation angle. Moreover, Genikomsou and Polak (2015) conducted a parameter analysis for dilation angles varying from 20° to 42°. However, the effect of the dilation angle was still an open issue. The dilation angles for different kinds of concretes were not unique. Therefore, a parametric analysis was conducted to investigate the influence of the dilation angle, which varied from 25° to 35°. Figure 24 shows the effect of the different dilation angles on the obtained load vs. displacement curves. The change in the dilation angle had no influence on the initial stiffness of the numerical model. However, when the load reached approximately 1500 kN, the stiffness of the numerical model began to increase with the dilation angle. Furthermore, when the dilation angle was less than 30°, the numerical results appeared to be unstable in the yielding stage, and an obvious fluctuation in the curves was observed. Overall, the numerical results depended on the choice of the dilation angle, but the influences could be negligible for a dilation angle varying from 30° to 35°, which showed the same tendency as Genikomsou and Polak (2015) conclusion. Therefore, in the following analyses, the dilation angle was set to 30°.

4.2 Effect of the Viscosity Parameter

Numerical modeling involving the softening behavior of a material and stiffness degradation can easily face convergence difficulties when the implicit FEM is implemented (ABAQUS Analysis User's Manual 2016). To improve the convergence, viscosity regularization technology
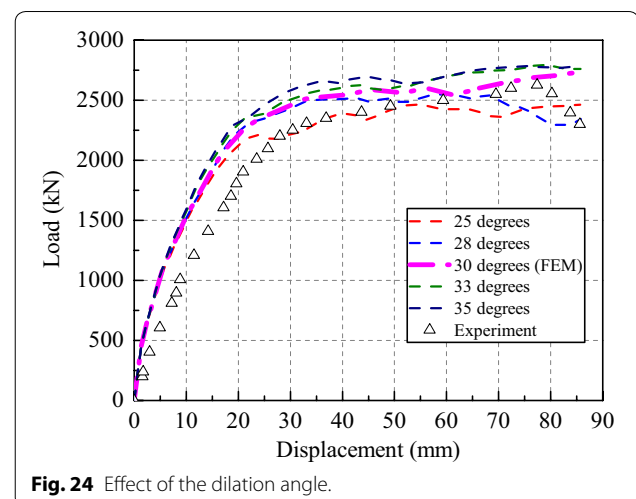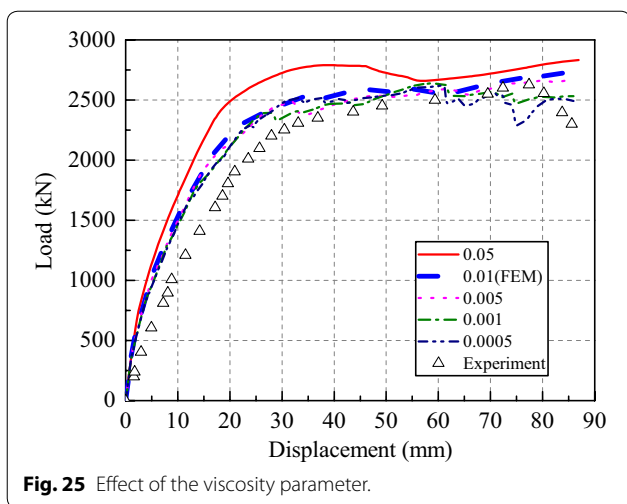

Fig. 24 Effect of the dilation angle.

Liu *et al. Int J Concr Struct Mater*   (2020) 14:36

Page 20 of 23

Fig. 25 Effect of the viscosity parameter.

was used in the CDP model. With a proper value of the viscosity parameter, the viscosity regularization technology helps to improve the convergence rate and does not compromise the results from the numerical modeling. In this subsection, the viscosity parameter was varied from 0.0005 s to 0.05 s to investigate its effect on the numerical results.

Figure 25 shows the various load–displacement curves obtained by the numerical modeling with different viscosity parameters. When the viscosity parameter exceeded 0.01 s, the stiffness of the specimen clearly increased with the increased ultimate bearing capacity. However, the changes in the stiffness of the specimen became negligible when the viscosity parameter decreased from 0.01 s to 0.0005 s. Moreover, when the viscosity parameter was less than 0.005 s, the load vs. displacement curves showed an instability after the yielding of the specimen, which was similar to the results obtained with a small dilation angle (mentioned in Subsection 4.1). The calculation time increased rapidly with the decrease of the viscosity parameter. For example, the calculation times for 0.05 s and 0.005 s were 375 min and 1568 min, respectively. The latter was approximately 4 times the former. Therefore, to complete the numerical calculation effectively and to obtain reasonable numerical results, the viscosity parameter should be selected carefully on the basis of parametric analysis. In all the following analyses, the viscosity parameter was set to 0.01 s.

4.3 Effect of the Axial Load on the Strut
Considering that the existence of axial loads on the strut could improve the bearing capacity of the joint, an axial load was not applied to the strut during the experimental testing so that the minimum bearing capacity could be obtained. However, in a practical engineering project,

the strut, as a part of the support system, must be able to bear an axial load. An axial compression ratio was defined here as the ratio of the axial load to be applied on the strut to the maximum axial load that the strut could bear. According to the design guidelines, the design axial load was 4604 kN, while the maximum axial load that the strut can bear was approximately 25,500 kN. In other words, the axial compression ratio was 0.18. Therefore, to investigate the influence of the axial load on the strut, the axial compression ratio was varied from 0.10 to 0.50 in the parameter analyses. Figure 26 depicts the load vs. displacement curves obtained from the numerical modeling with various axial compression ratios, in which N is the axial load, A_s is the area of the strut, and f_c is the design compressive strength of the concrete. Overall, as the axial compression ratio increased, the ultimate bearing capacity of the wall-beam-strut joint increased. However, a larger axial compression ratio could also cause the joint to reach a higher ultimate load at a smaller displacement loading. In other words, a larger axial compression ratio resulted in a worse ductility. Moreover, as presented in Table 4, although the axial force in the strut could improve the ultimate bearing capacity, the improvement was limited. The maximum improvement was approximately 9% when the axial compression ratio was varied between 0.18 and 0.30. When the axial compression ratio exceeded 0.30, the influence of the axial compression ratio seemed to be negligible. In summary, the numerical modeling of the effect of the axial load concluded that the axial forces could improve the ultimate bearing capacity but decrease the ductility, which was consistent with the observation of Behnam et al. (2018). Furthermore, an axial compression ratio beyond 0.3 had a negligible influence on the behavior of the joint.
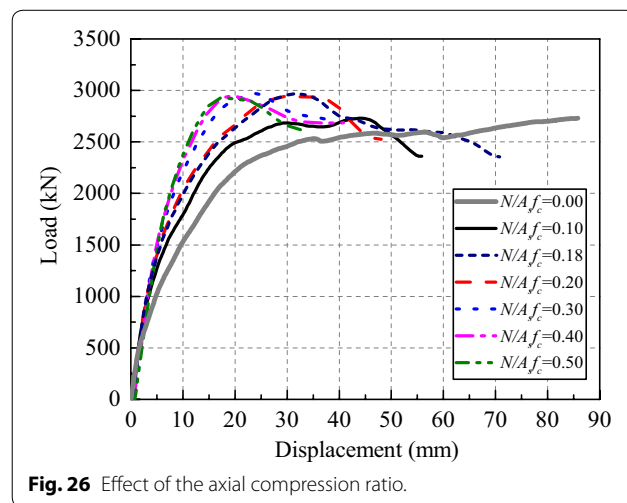

Fig. 26 Effect of the axial compression ratio.

Table 4 Ultimate bearing capacity for different axial compression ratios.

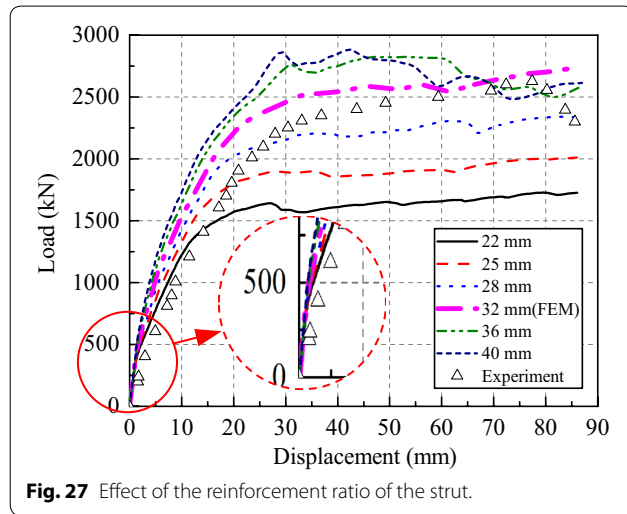| Axial compression ratio [$N/(A_s.f_c)$]	0	0.10	0.18	0.20	0.30	0.40	0.50
Ultimate bearing capacity (kN)	2730	2729	2966	2942	2970	2944	2928
Improvement (%)	–	0	8	9	9	8	7

Fig. 27 Effect of the reinforcement ratio of the strut.

4.4 Effect of the Reinforcement Ratio of the Strut

The reinforcement ratio of the cross-section of the strut in the experimental testing was approximately 3.0%, which was higher than the limit of 2.5% recommended by the design code of concrete structures in China, since the strut worked as a part of the joint. Moreover, denser rebars with larger diameters could cause an inconvenience during constructions. Therefore, to improve the construction efficiency and save resources, the influence of the reinforcement ratio on the ultimate bearing capacity of the joint was investigated, as illustrated in Fig. 27. As the diameter of the longitudinal rebars in the strut increased, the ultimate bearing capacity and the stiffness of the specimen increased. However, the diameter of the longitudinal rebars had little effect on the stiffness of the specimen before the load reached 500 kN, which revealed that the concrete bore most of the tension in this stage. As listed in Table 5, when the diameter of the rebars varied from 32 mm to 40 mm, the ultimate bearing capacity

of the joint had not been clearly improved. When the diameter of the rebars exceeded 32 mm, the concrete in the compressive area crushed before the rebars yielded. Overall, the design load for the strut was 816 kN, which was far lower than the minimum ultimate bearing capacity obtained from the numerical modeling with various reinforcement ratios. Consequently, from the viewpoint of reducing construction costs, the rebars used in practical engineering projects could be reduced in terms of the diameter or quantity.

5 Conclusion

This paper investigated the mechanical behavior of a wall-beam-strut joint proposed for a prefabricated underground construction under monotonic and cyclic loads through both full-scale experimental tests and three-dimensional nonlinear finite element modeling. The full-scale experimental tests focused on investigating the concrete cracking process and deflection of the joint under monotonic loading conditions and determining the failure pattern and skeleton curve of the joint under cyclic loading conditions. In the numerical simulations, the CDP model was adopted to simulate the complete stress–strain behavior of the concrete and the associated stiffness degradation, while the bilinear model was used to simulate the reinforcements embedded into the concrete in the wall-beam-strut joint. The load–displacement curves, cracking distributions and reinforcement strains from the numerical modeling of the wall-beam-strut joint under the monotonic loading conditions were compared with those from the experimental tests. Moreover, the skeleton curves from the numerical modeling of the joint under the cyclic loading condition were compared with those from the experimental tests.

The comparison indicates that the trends of the load–displacement curves obtained from the numerical

Table 5 Ultimate bearing capacity for different reinforcement ratios.

The diameter of the longitudinal rebars (mm)	22	25	28	32	36	40
Reinforcement ratio (%)	1.4	1.8	2.3	3.0	3.8	4.7
Ultimate bearing capacity (kN)	1727	2010	2330	2730	2823	2882
Improvement (%)	–	16	35	58	63	67

Liu *et al. Int J Concr Struct Mater*   (2020) 14:36

Page 22 of 23

simulation and experimental tests agree well. However, the cracking, yield and ultimate loads of the joints from the numerical modeling are 2.5% lower, 2.6% higher and 3.8% higher, respectively, than those from the experimental tests. Moreover, the numerical simulation can capture the concrete cracking process through the modeled distribution of the tensile damage in the early loading stage of the joint but fails to capture the specific crack distribution in later stages due to the accumulation of the tensile damage, although the cracking area can still be indicated by the distribution of the tensile damage. Furthermore, most of the reinforcement strains obtained from the numerical modeling show the same tendency as those from the experimental test, and their values are very similar before the joint yields, although it is difficult to compare their exact values after yielding.

In addition, the skeleton curves of the joint under the cyclic loading condition obtained from the numerical modeling show a greater stiffness than those from the experimental test, but the trends agree well. It is believed that the differences are because the materials in the numerical modelling are idealized without considering their discreteness, such as concrete discreteness, and the slippage between the reinforcements and concrete after concrete cracking is not included, which results in differences in the applied loads inside the concrete, as well as the inaccurate positioning of the strain gauges after concrete cracking.

Afterwards, a series of parametric analyses are conducted to investigate the effect of the dilatation angle, the viscosity parameter and the mesh size on the numerical modeling results and to further validate the results summarized above. Moreover, the effect of the axial load on the strut and the diameter of the longitudinal reinforcements in the strut on the bearing capacity of the joint are discussed. Finally, it is concluded from both the experimental tests and numerical modelings that the proposed wall-beam-strut joint has not only an ultimate bearing capacity that is at least 3 times higher than the design load but also a good ductility, thus satisfying the requirements for prefabricated underground construction. The parametric analyses further reveal that the diameter or quantity of the rebars can be reduced, which is beneficial in terms of reducing construction costs in practical engineering projects.

Acknowledgements
Not applicable.

Authors' contributions
TL and JL planned the experimental program, performed the experiments, analyzed the data, and drafted the paper. JL was in charge of the FE simulation and writing the paper. HL was in charge of analyzing the numerical results and writing the paper. All authors contributed to writing the paper. All authors read and approved the final manuscript.

Authors' information
Tingjin Liu, Associate Professor, State Key Laboratory of Subtropical Building Science, South China University of Technology, Guangzhou, 510640, China. Associate Professor, South China Institute of Geotechnical Engineering, South China University of Technology, Guangzhou 510640, China. Associate Professor, School of Civil Engineering and Transportation, South China University of Technology, Guangzhou 510640, China.

Jiandong Lu, Master's Student, School of Civil Engineering and Transportation, South China University of Technology, Guangzhou 510640, China.

Hongyuan Liu, Senior Lecturer, School of Engineering, University of Tasmania, Hobart, TAS 7001, Australia.

Availability of data and materials
The data in the paper will be supplied upon request.

Competing interests
The authors declare that they have no competing interests.

Author details
[1] State Key Laboratory of Subtropical Building Science, South China University of Technology, Guangzhou 510640, China. [2] South China Institute of Geotechnical Engineering, South China University of Technology, Guangzhou 510640, China. [3] School of Civil Engineering and Transportation, South China University of Technology, Guangzhou 510640, China. [4] School of Engineering, University of Tasmania, Hobart, TAS 7001, Australia.

References
ABAQUS Analysis User's Manual 6.14-3. (2016) Dassault Systemes Simulia Corp., Providence.

Ameli, M. J., & Pantelides, C. P. (2017). Seismic analysis of precast concrete bridge columns connected with grouted splice sleeve connectors. *Journal of Structural Engineering, 143*(2), 04016176.

Ameli, M. J., et al. (2015). Seismic evaluation of grouted splice sleeve connections for reinforced precast concrete column-to-cap beam joints in accelerated bridge construction. *PCI Journal, 60*(2), 80–103.

Ameli, M. J., et al. (2016). Seismic column-to-footing connections using grouted splice sleeves. *ACI Structural Journal, 113*(5), 1021.

Behnam, H., Kuang, J. S., & Samali, B. (2018). Parametric finite element analysis of RC wide beam-column connections. *Computers & Structures, 205,* 28–44.

Bompa, D. V., & Elghazouli, A. Y. (2017). Ductility considerations for mechanical reinforcement couplers. In *Structures* (Vol. 12, pp. 115–119). Elsevier.

Bompa, D. V., & Elghazouli, A. Y. (2018). Monotonic and cyclic performance of threaded reinforcement splices. In *Structures* (Vol. 16, pp. 358–372). Elsevier.

Bompa, D. V., & Elghazouli, A. Y. (2019). Inelastic cyclic behaviour of RC members incorporating threaded reinforcement couplers. *Engineering Structures, 180,* 468–483.

Chidambaram, R. S., & Agarwal, P. (2018). Performance evaluation of innovative hybrid rebar coupler in reinforced concrete beams subjected to monotonic loading. *Structural Concrete, 19*(3), 892–903.

dos Santos, L. R., de Sousa Cardoso, H., Caldas, R. B., & Grilo, L. F. (2020). Finite element model for bolted shear connectors in concrete-filled steel tubular columns. *Engineering Structures, 203,* 109863.

Genikomsou, A. S., & Polak, M. A. (2015). Finite element analysis of punching shear of concrete slabs using damaged plasticity model in ABAQUS. *Engineering Structures, 98,* 38–48.

Liu *et al. Int J Concr Struct Mater*   *(2020) 14:36*

Page 23 of 23

Haber, Z. B., Saiidi, M. S., & Sanders, D. H. (2014). Seismic performance of precast columns with mechanically spliced column-footing connections. *ACI Structural Journal, 111*(3), 639–650.

Kazemi, M., Li, J., Harehdasht, S. L., Yousefieh, N., Jahandari, S., & Saberian, M. (2020). Non-linear behaviour of concrete beams reinforced with GFRP and CFRP bars grouted in sleeves. In *Structures* (Vol. 23, pp. 87–102). Elsevier.

Liu, M., Jia, S., & Liu, X. (2019a). Evaluation of mitigation potential of GHG emissions from the construction of prefabricated subway station. *Journal of Cleaner Production, 236,* 117700.

Liu, J., Peng, Q., Chen, J., & Yin, Y. (2019b). Connectivity reliability on an urban rail transit network from the perspective of passenger travel. *Urban Rail Transit, 6,* 1–14.

Liu, T., Lu, J. et al. (2020) Experimental investigation on mechanical behavior of wall-beam-strut joints of a prefabricated underground construction. *International Journal of Concrete Structures and Materials* **(Under Review)**

Lu, L. H., Wang, W. T., Wang, G. F., Xu, Q. W., & Wang, Y. J. (2018). Experimental Study on the Mechanical Properties and Deformation Characteristics of Prefabricated Concrete Square Pile. In *GeoShanghai International Conference* pp. 520–527). Springer, Singapore.

Nana, W. S. A., Bui, T. T., Limam, A., & Abouri, S. (2017). Experimental and numerical modelling of shear behaviour of full-scale RC slabs under concentrated loads. In *Structures* (Vol. 10, pp. 96–116). Elsevier.

Sidoroff, F. (1981). Description of anisotropic damage application to elasticity. In *Physical Non-Linearities in Structural Analysis* (pp. 237–244). Springer, Berlin, Heidelberg.

Wang, H., Marino, E. M., & Pan, P. (2019). Design, testing and finite element analysis of an improved precast prestressed beam-to-column joint. *Engineering Structures, 199,* 109661.

Wosatko, A., Winnicki, A., Polak, M. A., & Pamin, J. (2019). Role of dilatancy angle in plasticity-based models of concrete. *Archives of Civil and Mechanical Engineering, 19*(4), 1268–1283.

Wu, R.-Y., & Pantelides, C. P. (2018). Concentrated and distributed plasticity models for seismic repair of damaged RC bridge columns. *Journal of Composites for Construction, 22*(5), 04018044.

Xiu, C. H., Li, H., Wang, W. X., & Xu, Q. W. (2018). Study on the Force and Deformation Characteristics of Prefabricated Pile-Wall Compound Structure and Its Application in Foundation Pit Engineering. In *GeoShanghai International Conference* (pp. 503–510). Springer, Singapore.

Yang, X., Huang, M., & Lin, F. (2019a) Research strategies on new prefabricated technology for underground metro stations. *Urban Rail Transit*, 1–10.

Yang, X., Shi, Z., & Lin, F. (2019b). Research on shear capacity and checking method of MT·G-joint for application in prefabricated underground structures. *Advances in Materials Science and Engineering, 2019.*

Zhang, L., Long, R., & Chen, H. (2019). Carbon emission reduction potential of urban rail transit in China based on electricity consumption structure. *Resources, Conservation and Recycling, 142,* 113–121.

Publisher's Note